Spectroscopic Studies of Metal Complexes with Large Magnetic Anisotropy

A Thesis Presented for the

Master of Science

Degree

The University of Tennessee, Knoxville

Chelsea Natasha Widener

August 2020

DEDICATION

To my little sisters.

I hope all your dreams come true

ACKNOWLEDGEMENTS

I would like to acknowledge my advisor, Dr. Ziling (Ben) Xue for his guidance, support, and understanding during my time in graduate school. I would also like to acknowledge Dr. Sheng Dai, Dr. John Brantley, Dr. Craig Barnes, and Dr. Dustin Gilbert as my graduate committee members.

I would like to thank Dr. Luke Daemen and Dr. Yongqiang Cheng at Oak Ridge National Laboratory (ORNL) for their assistance with inelastic neutron scattering (INS) and phonon computations. I would also like to thank Dr. Dmitry Smirnov, Dr. Komalavalli Thirunavukkuarasu, Dr. Mykhaylo Ozerov, Rachel Richardson, and Zhengguang Lu of the National High Magnetic Field Laboratory for their help with far-IR and Raman spectroscopic studies.

I would like to thank Dr. Duncan Moseley for passing on his knowledge of synthesis, spectroscopy, and data analysis techniques. I would also like to acknowledge the assistance provided by my fellow group members, past and present: Dr. Shelby Stavretis, Zhiming Liu, Peter Pham, Alexandria Bone, Pagnareach (Reach) Tin, Brian Kettell, and Adam Hand.

I would like to acknowledge the National Science Foundation for the support of my research, ORNL and the Department of Energy for allowing me to use the Spallation Neutron Source for my neutron scattering and computational work, and the National High Magnetic Field Laboratory and the State of Florida

for allowing me to use their magnets and instruments to perform far-IR and Raman studies.

Finally, I would like to thank my family and friends for their love, support, and encouragement. Without them, I could never have made it this far.

ABSTRACT

Single-molecule magnets are known for their high uniaxial anisotropy and slow magnetic relaxation. Trigonal bipyramidal Ni(II) complex $[Ni(Me_6tren)Cl](ClO_4)$ (**1**, Me_6tren = tris[2-(dimethylamino)ethyl]amine) has recently been shown to possess large, uniaxial magnetic anisotropy. Direct observation of the transitions between Zeeman-split states in far-IR magnetospectrocopy (FIRMS) gives the axial ZFS parameter D = -110.7(3) cm^{-1}. Hirshfeld surface analysis of the crystal structure of **1** has been performed, revealing the interactions between the cation and anion in a molecule of **1** as well as among the molecules of **1** in crystals. $Dy(acac)_3(H_2O)_2$ (**2**, acac = acetylacetonate) is a Dy(III) complex with distorted D_{4d} symmetry. It has a high barrier to magnetic relaxation due to its electron. A magnetic peak is identified at 175.5 cm^{-1} and there is evidence of another peak observed in FIRMS. Multiple phonons are identified and avoided crossings that are characteristic of spin-phonon coupling are evident. Although inelastic neutron scattering (INS) alone cannot identify the magnetic peak in this case, the 0 K spectrum calculated with Vienna Ab-initio Simulation Package (VASP) does agree with experimental INS spectrum at 5 K. Furthermore, the irreducible representation of each phonon was identified. Yb(trensal) [**3**, H_3trensal = 2,2',2"-tris(salicylideneimino)trimethylamine] is a 7-coordinate, S = 1/2 Yb(III) complex with C_{3v} local symmetry. The far-IR spectrum shows a distinct repetitive pattern that needs further investigation and

modelling to explain. If a magnetic peak could be identified via far-IR and/or inelastic scattering neutron (INS) spectroscopy would be helpful in confirming the magnetic peak, but INS cannot be used as a stand-alone identifier in this case. Furthermore, there is disagreement between the calculated and experimental spectra at low frequency and many of the irreducible representations cannot be computed based upon the complexity of the molecule and its interactions. Both **2** and **3** have complicated magnetic properties which are difficult to model and will require additional studies in the future.

TABLE OF CONTENTS

Chapter 1. Introduction 1

1.1. Single-molecule magnets 2

1.2. Transition-metal vs. lanthanide-based SMMs 5

1.3. Magnetic relaxation 9

1.4. Spectroscopic studies 13

1.4.1. Far-IR magnetospectroscopy (FIRMS) 14

1.4.2. Raman under magnetic field 15

1.4.3. Inelastic neutron scattering (INS) 16

1.5. Phonon computations and simulations of INS spectra 17

1.6. Hirshfeld surface calculations 18

1.7. Overview of the thesis 19

Chapter 2. Direct determination of large axial anisotropy in a nickel(II) complex 21

2.1. Abstract 23

2.2. Introduction 23

2.3. Experimental 27

2.3.1. Synthesis 27

2.3.2. Far-IR studies 28

2.3.3. Raman studies 28

2.3.4. Hirshfeld surface calculation 30
2.4. Results and discussion 30
2.4.1. FIRMS studies 30
2.4.2. Raman spectra 33
2.4.3. Hirshfeld surface analyses 35
2.5 Conclusions 39

Chapter 3. Spectroscopic properties of a dysprosium(III) single-molecule magnet complex 41
3.1. Abstract 42
3.2. Introduction 42
3.3. Experimental 46
3.3.1. Synthesis 46
3.3.2. FIRMS studies 46
3.3.3. Raman studies 48
3.3.4. INS study and phonon computations 48
3.4. Results and discussion 49
3.4.1. FIRMS studies 49
3.4.2. Raman magnetospectroscopic studies 55
3.4.3. INS study and phonon computations 55
3.5 Conclusions 59

Chapter 4. Spectroscopic properties of a ytterbium(III) single-molecule magnet complex 61
4.1. Abstract 62
4.2. Introduction 62
4.3. Experimental 65
4.3.1. Synthesis 65
4.3.2. FIRMS study 65
4.3.3. Raman magnetospectroscopic study 66
4.3.4. INS study and computations 66
4.4. Results and discussion 68
4.4.1. FIRMS study 68
4.4.2. Raman magnetospectroscopic study 72
4.4.3. INS study and phonon computations 72

Chapter 5. Future work 77

References 80

Appendix 96

Vita 100

LIST OF TABLES

Table 2.1. Volumes and surface areas in **2** from Hirshfeld surface analyses.....37

Table 3.1. Animated phonons in $Dy(acac)_3(H_2O)_2$ (**3**) from VASP calculations...60

Table 4.1. Animated phonons in Yb(trensal) (**4**) from VASP calculations 76

LIST OF FIGURES

Figure 1.1. Schematic energy barrier of a system with spin (*S*) 4

Figure 1.2. ZFS configuration of a d^7 complex in a D_{4h} ligand field 7

Figure 1.3. Low energy electronic structure of the Dy(III) ion with sequential perturbations of electron-electron repulsions, spin–orbit coupling, and the crystal field 8

Figure 1.4. Quadrupole approximations of the 4f-shell electron distribution for the tripositive lanthanides (Top). Depictions of low- and high-energy configurations of the f-orbital electron density with respect to the crystal field environment for a 4f ion of oblate (Bottom-Left) and prolate (Bottom-Right) electron density 10

Figure 1.5. Comparison of direct, 1st-order Raman, Orbach, and 2nd-order Raman relaxation mechanisms 12

Figure 2.1. (Left) $[Ni(Me_6tren)Cl]^+$ cation in **2** with local C_{3v} symmetry. (Right) View of the cation and anion in **2** looking down the crystallographic *c* axis, showing that the cation is on a C_3 axis. (Bottom) Splitting of the d orbitals in the $[Ni(Me_6tren)Cl]^+$ cation 25

Figure 2.2. Ground-state triplet levels in high-spin, d^8 complexes with C_{3v} symmetry and uniaxial magnetic anisotropy ($D < 0$) 26

Figure 2.3. Photos of the samples of **2** for far-IR (Left) and Raman (Right) spectroscopic studies. 29

Figure 2.4. (Top) Far-IR spectra of **2** at 0 and 17 T magnetic fields. (Bottom) Contour map of normalized transmission in 0–17 T magnetic fields by the Filled Contour Plot in SigmaPlot 2000 31

Figure 2.5. (Top) Raman spectra of **2** at 5 K and 0-12 T external magnetic fields. (Bottom) Contour plot of the Raman spectra at 0-12 T magnetic fields 34

Figure 2.6. Hirshfeld surface of **2** showing normalized close distances of the pro-molecule at 100(1) K.....36

Figure 2.7. Hirshfeld fingerprint plots. 38

Figure 3.1. Relaxation pathways derived from ab-initio calculations of a fused-ring Dy(III) SMM where darker lines mean larger contribution to the overall relaxation 44

Figure 3.2. $Dy(acac)_3(H_2O)_2$ (**3**): (Left) Structure and (Right) View of **3** looking down the crystallographic *c* axis. 45

Figure 3.3. Photos of the samples of **3** for (Left) powder far-IR, (Middle) single-crystal far-IR, and (Right) Raman spectroscopic studies. 47

Figure 3.4. (Top) Far-IR spectra of **3** at 0 and 17 T magnetic fields. (Middle) Transmission normalized to the zero-field spectrum T_B/T_0 at 1-17 T. (Bottom) Contour map of normalized transmission in 0-17 T magnetic fields by the Filled Contour Plot in SigmaPlot 2000 50

Figure 3.5. (Top) Far-IR spectra of a single crystal of **3-*d*$_4$** at 0 and 17.5 T magnetic fields. (Middle) Transmission normalized to the zero-field spectrum

T_B/T_0 at 1-17 T. (Bottom) Contour map of normalized transmission in 0-17 T magnetic fields by the Filled Contour Plot in SigmaPlot 2000.....51

Figure 3.6. (Top) Far-IR spectra of **3-*d*$_{25}$** at 0 and 17 T magnetic fields. (Middle) Transmission normalized to the zero-field spectrum T_B/T_0 at 1-17 T. (Bottom) Contour map of normalized transmission in 0-17 T magnetic fields by the Filled Contour Plot in SigmaPlot 2000 52

Figure 3.7. Raman spectra of **3** at 4.5 K and 0-17 T external magnetic fields 56

Figure 3.8. Raman spectra of **3-*d*$_{25}$** at 4.5 K and 0-17 T external magnetic fields. 57

Figure 3.9. INS spectra of **3** at 5, 25, 50, 75, 100, 125 and 150 K on VISION. Calculated INS spectrum by VASP is shown in grey for comparison.....58

Figure 4.1. (Top) Structure of Yb(trensal) (**4**), (Middle) Energy splitting diagram (Bottom) View (looking down the *c* axis) of a molecule of **4** in its crystallographic unit cell; *a* axis: Pointing to the top; *b* axis: Pointing to the left.....63

Figure 4.2. (Left) Photo of a mosaic of crystals of **4** for far-IR spectroscopy; (Right) Photo of the sample of **4** for Raman magnetospectroscopy.....67

Figure 4.3. (Top) Far-IR spectra of a mosaic of crystals of **4**. (Middle) Transmission normalized to the zero-field spectrum T_B/T_0 at 1-17 T. (Bottom) Contour map of normalized transmission in 0-17 T magnetic fields by the Filled Contour Plot in SigmaPlot 2000. 69

Figure 4.4. (Top) Far-IR spectra of a power sample of **4**. (Middle) Transmission normalized to the zero-field spectrum T_B/T_0 at 1-17 T. (Bottom) Contour map of normalized transmission in 0-17 T magnetic fields by the Filled Contour Plot in SigmaPlot 2000 71

Figure 4.5. Raman spectra of Yb(trensal) (**4**) under external magnetic fields. 73

Figure 4.6. INS spectra of **4** at 5, 25, 50, 75, 100, 125 and 150 K on VISION. Calculated 0 K INS spectrum by VASP in grey for comparison. 75

Figure A1. Transmission FIRMS of **2** normalized to the zero-field spectrum T_B/T_0 at 1-17 T. 97

Figure A2. Additional top view of the Hirshfeld surface of **2** showing the packing diagram. 98

Figure A3. Additional side view of the Hirshfeld surface of **2** showing the packing diagram. 99

LIST OF ATTACHMENTS

Animation 1	1_Complex 3_104.69_Au.mp4
Animation 2	2_Complex 3_121.97_Au.mp4
Animation 3	3_Complex 3_143.79_Ag.mp4
Animation 4	4_Complex 3_169.21_Bg.mp4
Animation 5	5_Complex 3_194.98_Bu.mp4
Animation 6	6_Complex 3_221.53_Bg.mp4
Animation 7	7_Complex 3_241.14_Bg.mp4
Animation 8	8_Complex 3_255.82_Au.mp4
Animation 9	9_Complex 4_371.43_Bu.mp4
Animation 10	10_Complex 4_384.53.mp4
Animation 11	11_Complex 4_407.09_Ag.mp4
Animation 12	12_Complex 4_423.65.mp4
Animation 13	13_Complex 4_456.15.mp4
Animation 14	14_Complex 4_489.98_Bu.mp4
Animation 15	15_Complex 4_554.67_Au.mp4
Animation 16	16_Complex 4_571.57.mp4

LIST OF COMPOUNDS

$Co(acac)_2(H_2O)_2$	**1**
$Co(acac)_2(D_2O)_2$	**1-*d*$_4$**
$Co(acac\text{-}d_7)_2(D_2O)_2$	**1-*d*$_{18}$**
$[Ni(Me_6tren)Cl](ClO_4)$	**2**
$Dy(acac)_3(H_2O)_2$	**3**
$Dy(acac)_3(D_2O)_2$	**3-*d*$_4$**
$Dy(acac\text{-}d_7)_3(H_2O)_2$	**3-*d*$_{21}$**
$Dy(acac\text{-}d_7)_3(D_2O)_2$	**3-*d*$_{25}$**
Yb(trensal)	**4**

LIST OF ABBREVIATIONS

Back scattering (BS)

Cambridge Crystallographic Data Center (CCDC)

Charge-coupled device (CCD)

Crystallographic information file (CIF)

Electron magnetic resonance (EMR)

Far-infrared magnetospectroscopy (FIRMS)

Forward scattering (FS)

High-field/high-frequency electron paramagnetic resonance (HF-EPR)

Inelastic neutron scattering (INS)

Kramers doublets (KDs)

National High Magnetic Field Laboratory (NHFML)

Oak Ridge National Laboratory (ORNL)

Quantum bits (qubits)

Quantum tunneling of magnetization (QTM)

Single-ion magnet (SIM)

Single-molecule magnets (SMMs)

Spin-orbit coupling (SOC)

Spallation Neutron Source (SNS)

Super-conducting magnet (SCM)

Variable temperature (VT)

Vienna Ab-initio Simulation Package (VASP)

Zero-field splitting (ZFS)

CHAPTER 1. INTRODUCTION

1.1. Single-molecule magnets

Single-molecule magnets (SMMs) consist of metalorganic compounds which exhibit superparamagnetic behavior, the ability to change spins, below a certain blocking temperature (T_B). Below this temperature, these molecules exhibit hysteresis or alignment of their magnetic dipoles to an external magnetic field.[1] This alignment occurs in the most energetically favorable direction, the easy–axis (*z* direction) or –plane (*x,y* direction), and results in magnetic anisotropy.[2] The alignment remains even after the external field is removed due to the presence of an effective energy barrier to reversal (U_{eff}). SMMs typically have a high-spin metal center, large magnetic anisotropy, and a bistable electronic ground state. One particular type of SMMs is the single-ion magnets (SIMs) which typically consist of one metal center with unpaired electrons as opposed to a metal cluster.[1]

Prospective uses for SMMs include high-density data storage, molecular spintronics, and quantum computing. Spintronics takes advantage of spin properties of electrons to improve upon traditional electronics based the charges of electrons. SMMs would be the components for a spintronic circuit and could be used to create molecular spin valves as well as spin transistors.[3] In addition to storing and retrieving data, SMMs with molecules spaced far enough apart to prevent intermolecular interactions provide promise for information processing as well. The quantum properties such as superposition and entanglement which

these compounds possess are necessary for quantum bits (qubits) used in quantum computers.[4]

In order to make the more widespread use of SMMs, we need to first overcome hurdles such as the low temperature required for SMMs to retain their magnetization, the sensitivity of these compounds to magnetic fields and radiation, and the need for a reliable way to deposit and address single molecules. Typically, the blocking temperature for SMMs tend to be very low (below the boiling point of liquid nitrogen) making cooling the molecules prohibitively expensive. Even below the blocking temperature, stray radiation may be enough to overcome the effective barrier and allow for spin-reversal. Molecules with higher magnetic anisotropy have larger energy barriers to prevent spin reversal (Figure 1.1).[5] Therefore, SMMs need to have higher blocking temperatures as well as high anisotropy. Another challenge is the sensitivity of SMMs to external magnetic fields. If the field is large enough, it will magnetize or re-magnetize the molecule which could result in the loss of previously stored information. Even if these issues are addressed, we will still need to be able to deposit the molecules in designated positions and address specific molecules in order to efficiently store and retrieve data. The current work focuses on probing the spin-lattice interactions in SMMs.

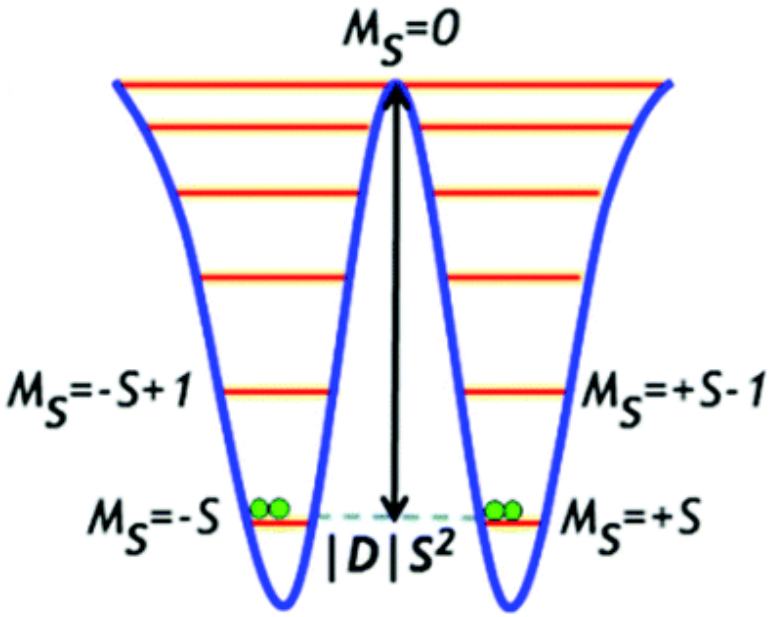

Figure 1.1. Schematic energy barrier of a system with spin (*S*). The two wells represent two spin states. Reproduced from Ref. 5 with permission from the Royal Society of Chemistry.

1.2. Transition-metal vs. lanthanide-based SMMs

Magnetic properties of transition metal complexes have been actively studied recently in part to understand the fundamental nature of the complexes and in part to probe their potential applications as SMMs and chemical qubits.[2, 6-23] For these SMMs, the orbital angular momentum can be quenched or unquenched. Unquenched angular momentum results when there are two or more degenerate orbitals that an electron can move between.[6] Such complexes typically have first-order SOC, often giving large separations of the SOC levels. Even if the symmetry of the molecule predicts unquenched angular momentum, Jahn-Teller distortions resulting from slight imperfections in the geometry may lift the degeneracy of the states, thereby quenching the orbital angular momentum.

For quenched angular momentum, where the electrons cannot orbit the molecule because there are no suitable orbitals do so (as degenerate states are all half-filled or fully-filled). In this case, 2nd order spin-orbit coupling (SOC) occurs.[2, 6-12, 14-20, 22-24] Here, the anisotropy barrier U is based on the ground state spin S and axial zero-field splitting (ZFS) parameter D. When S is an integer, $U = |D|S^2$ and when S is a half-integer $U = |D|(S^2 – 1/4)$. While D can be positive or negative, SMM behavior is typically observed when $D < 0$ because the transition between ground magnetic levels is forbidden (largest M_S levels are lower in energy when $D < 0$). However, there are well-known exceptions where D is positive for a complex and slow magnetic relaxation still occurs for the complex. The rhombic ZFS parameter E affects the magnetic relaxation of the SMMs.

When $E \neq 0$, different M_S states (such as $M_S = \pm 3/2$ and $\pm 1/2$) can mix. Such mixing may make transitions between $M_S = -3/2$ and $+3/2$ states, which are not normally allowed, occur. These ZFS parameters are terms found in the spin-Hamiltonian:[7, 25]

$$H = D\left(\hat{S}_z^2 - \frac{S(S+1)}{3}\right) + E\left(\hat{S}_x^2 - \hat{S}_y^2\right) + \mu_B g \hat{S} \cdot \hat{H} \qquad \text{(Eq. 2.1)}$$

where μ_B is the Bohr magneton, $\hat{S}$ is the spin operator, $\hat{H}$ is the magnetic field vectors.

Both *D* and *E* parameters serve to lift the degeneracy of the $2S + 1$ ($S > 1/2$) microstates, M_S, in the absence of magnetic field.[26] For transition metal-based SIMs, research has been directed at making complexes with large anisotropy *D* (Figure 1.2).

For lanthanide compounds, f orbitals are buried in the metals, forming weak bonds with ligands, making the ligand field typically weak and the metal-ligand bonds ionic in nature.[19] For these complexes, the crystal field is normally weaker than spin-orbital coupling (SOC), as the example in Figure 1.3 shows.[2] Thus, SOC is considered first, giving, *e.g.*, $^6H_{15/2}$ as the ground state for the Dy(III) ion. Upon the formation of complexes with ligands, the crystal field further splits the ground states (Figure 1.3).[1] This large SOC is the main feature of f-element based SMMs.[27-30]

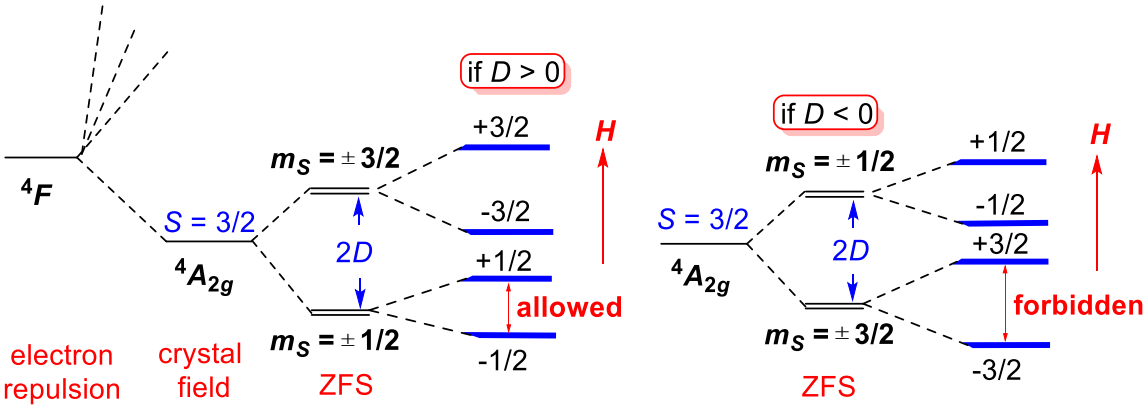

Figure 1.2. ZFS configuration of a d^7 complex in a D_{4h} ligand field.

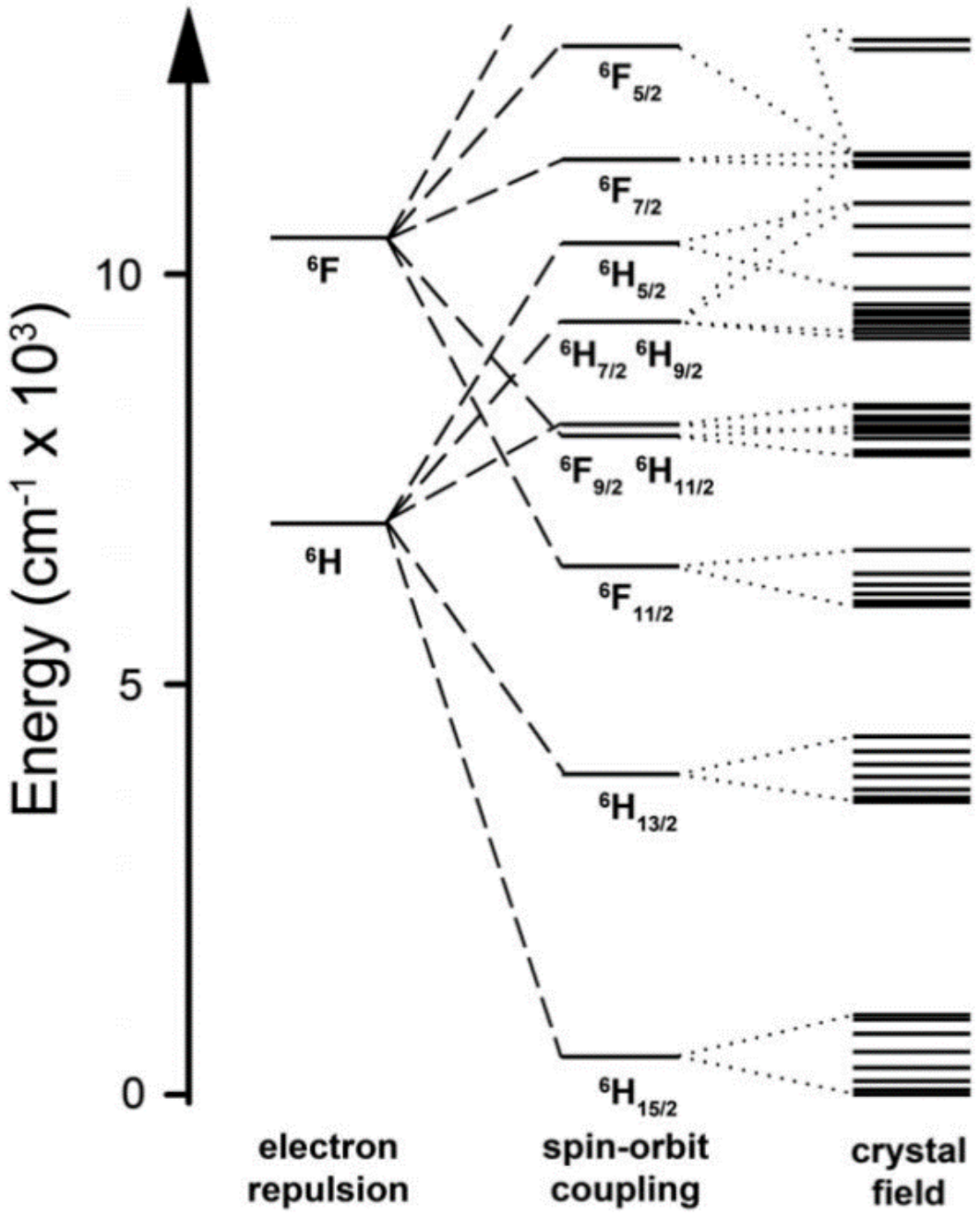

Figure 1.3. Low energy electronic structure of the Dy(III) ion with sequential perturbations of electron-electron repulsions, spin–orbit coupling, and the crystal field. Reproduced from Ref. 19 with permission from the Royal Society of Chemistry.

Using the Hamiltonian, $H = H_{\text{free ion}} + H_{\text{crystal field}}$, we can determine the crystal field structure which will give the optimal SMM behavior for a given lanthanide complex. The basic shapes for the lowest *J* states in an axial reference frame are described mathematically by the quadrupole moment of the f-electron charge cloud which can be oblate, prolate, or isotropic. The shape of this cloud depends upon the strong angular dependence of f orbitals, as depicted in Figure 1.4.[19] Oblate ions have the largest anisotropy when placed in a crystal field with the ligand electron density being concentrated above and below the *x*,*y*-plane. Prolate ions have increased anisotropy with an equatorially-coordinated geometry. Isotropic ions tend to have highest anisotropy with a high-symmetry ligand field. These geometries will minimize the repulsion between ligand and f-electron charge clouds (Figure 1.4).[19] This approach explains the prominence of axial and equatorial-coordinating ligands in lanthanide complexes as well as suggesting a method for making SMMs with strong single-ion anisotropy form strongly prolate ions.[19] For example, Er(III) and Dy(III) ions are typically present in complexes with SIM properties which are both highly anisotropic.[19]

1.3. Magnetic relaxation

For SMMs, phonons within a certain range can interact with the magnetic moment, providing an outlet for spin-reversal below *U*. This lower energy relaxation U_{eff} is allowed by spin-phonon coupling and governed by Eq. 2:[2, 31, 32]

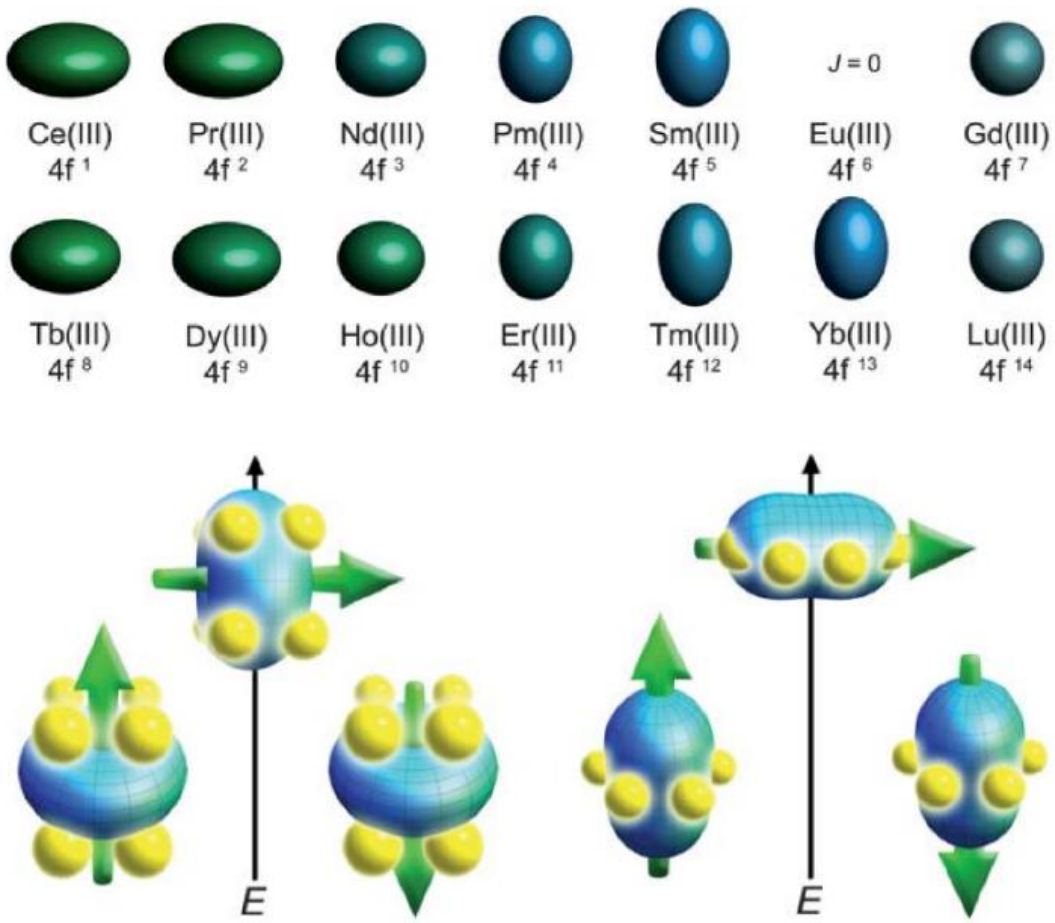

Figure 1.4. Quadrupole approximations of the 4f-shell electron distribution for the tripositive lanthanides (Top). Depictions of low- and high-energy configurations of the f-orbital electron density with respect to the crystal field environment for a 4f ion of oblate (Bottom-Left) and prolate (Bottom-Right) electron density. The green arrow represents the orientation of the spin angular momentum coupled to the orbital moment. Reproduced from Ref. 19 with permission from the Royal Society of Chemistry.

$$\tau^{-1} = AH^{n1}T + CT^{n2} + \tau_0^{-1} + \tau_{\text{QTM}}^{-1} \qquad \text{(Eq. 2.2)}$$

Here, A, C, and τ_0^{-1} are parameters related to the spin-phonon coupling matrix and the speed of sound while T is temperature, k_B is the Boltzmann constant, n_1 and n_2 are values that can be found in the literature, and QTM refers to quantum tunneling of magnetization.[33]

The four terms of this equation correspond to the four different types of relaxation. The first is a transition from the spin-excited state to the ground state with the emitted energy taken up by the lattice as a phonon which is known as a direct relaxation (Figure 1.5).[32] These transitions are typically very small in energy and are only prominent below the liquid helium temperature since very few phonons are present at these low energy levels. Direct transitions are known as single phonon processes because they only involve a single transition from one state to another.

The second type of relaxation involves two phonons and is known as a Raman process.[32] When the molecule relaxes in a first-order Raman process, the energy is taken up by a superposition of two phonons. The energy released by relaxation will match the difference between the energies of these two phonons. The dashed line here represents a virtual intermediate state. In the second-order Raman process, the molecule is excited to a second virtual state before relaxing to the ground state. Otherwise, it is the same as the first-order process.

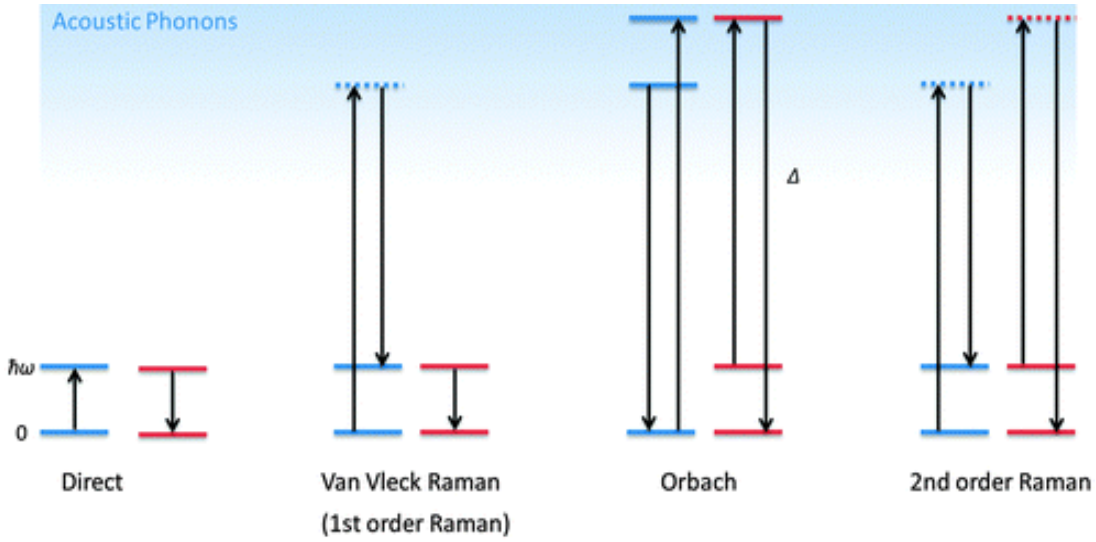

Figure 1.5. Comparison of direct, 1st-order Raman, Orbach, and 2nd-order Raman relaxation mechanisms. Reproduced from Ref. 32 with permission from the Royal Society of Chemistry.

The third type is the Orbach process wherein a phonon is absorbed to reach a low energy excited state of the molecule.[32] This excited state will then emit a phonon and relax back to the ground state.

The fourth type of relaxation, QTM, disrupts SMM behavior. The direct and Raman processes tend to dominate the transition-metal relaxation process for SMMs, since the Orbach term is several times smaller at low temperatures and the relaxation process involves many transitions between M_S states. On the other hand, relaxation in f-element SMMs occurs entirely through Raman, Orbach, and quantum tunneling pathways at low temperatures.[31]

1.4. Spectroscopic studies

In order to represent the direct, Raman, Orbach, and QTM relaxation mechanisms, a minimum of six parameters are needed. However, no single technique can adequately address so many parameters.[34] Therefore, a variety of techniques are used to characterize the magnetic relaxation. Under certain experimental conditions, some relaxation mechanisms can be excluded. For example, Kramers ions will not undergo the direct process without an external magnetic field. Single crystal magnetic susceptibility is also commonly used as an indirect method of determining the magnetic barrier. However, it cannot be used to measure the energies between ground and excited magnetic excited states or the spin-phonon couplings that lead to magnetic relaxation. In order to probe magnetic excited states, we have utilized far-IR magnetospectroscopy

(FIRMS), Raman magnetospectroscopy, and inelastic neutron spectroscopy (INS). Phonon calculations have also been used in our studies to obtain phonon properties of the solids of the SMMs.[34]

1.4.1. Far-IR magnetospectroscopy (FIRMS)

Far-IR spectroscopy can be used to determine the transition between the ground and excited states of a complex in the far-IR range (~10-667 cm^{-1} or 0.3-20.0 THz).[35, 36] FIRMS involves sweeping in the frequency domain (down to 20 cm^{-1}) while the magnetic field is fixed [in contract to the electron paramagnetic resonance (EPR), where the frequency is fixed and magnetic field is swept]. FIRMS is a direct technique to probe transitions such as those among ZFS states in transition metal complexes and magnetic transitions in f-element complexes.[14, 37-46] It involves the use of magnetic fields in probing a sample by far-IR spectroscopy.[37-39, 47, 48]

For d-complexes with unquenched orbital angular momenta and f-complexes, transitions among the first-order SOC states may be electric-dipole or magnetic-dipole allowed, although the electric-dipole allowed transitions are typically much stronger. For d-compounds with quenched orbital angular momenta (and thus second-order SOC), earlier work by Brackett and Richards demonstrated that transitions among the ZFS states are magnetic-dipole allowed.[47] Thus, the ZFS splitting can be directly measured with far-IR spectroscopy.[47] In FIRMS, the sample is placed in variable magnetic

fields.[37-39, 47, 48] The Zeeman effect on the magnetic levels shifts the magnetic peaks in FIRMS, thus helping reveal and identify magnetic transitions in metal complexes that are too large to be measured by high-field/high-frequency electron paramagnetic resonance (HF-EPR). This ability to obtain both frequency and field information over a relatively wide range is the main advantage of using far-IR under magnetic fields.[37-39, 47-49] For example, our group has recently used far-IR and Raman spectroscopies to report distinct spin-phonon coupling for $Co(acac)_2(H_2O)_2$ (**1**) and two of its deuterated isotopologues, $Co(acac)_2(D_2O)_2$ (**1-*d*$_4$**) and $Co(acac\text{-}d_7)_2(D_2O)_2$ (**1-*d*$_{18}$**).[38] When increasing the external magnetic field, we observed a magnetic-dipole-allowed, inter-Kramers-doublet $M_S = \pm 1/2 \rightarrow \pm 3/2$ transition shifting to higher energy. Our group has also used far-IR to probe the transitions between Kramers doublets (KDs) in an f-complex, SMM $Er[N(SiMe_3)_2]_3$.[49]

1.4.2. Raman under magnetic field

Raman spectroscopy, a light-scattering technique based upon exciting an electron to a higher virtual state and allowing the particle to relax back to a different vibrational or electronic state in the ground electronic state, can also be used to determine the energies of the excited states.[50] For lanthanide complexes and d complexes with the first-order SOC, their states have both orbital components and transitions among them are considered as electronic. Such electronic Raman spectroscopy has been studied.[51, 52] However, regarding

Raman for ZFS transitions, whether or not it is intrinsically allowed is still not well-understood. While magnetic peaks themselves are not visible in Raman spectroscopy, it is possible to observe changes in the phonons resulting from changes in the magnetic field as well as spin-phonon coupling (interactions between the magnetic peak and phonons). In the Raman study of **1** and its deuterated isotopologues, the spin-phonon coupling was observed as avoided crossings with coupling constants of 1-2 cm^{-1}.[38]

1.4.3. Inelastic neutron scattering (INS)

INS is used to study atomic/molecular motion as well as magnetic and electronic excitations.[53] Since neutrons have a spin, they carry a magnetic moment.[54] The magnetic field created by unpaired electrons in a sample interacts with this magnetic moment causing the incident neutrons to be scattered. The resulting spectrum gives a direct measurement of the excitations corresponding to allowed transitions between M_S or M_J sublevels for the atoms.[26]

Neutrons may interact with nuclei of atoms as well, the probability of which is measured by the cross section of the atoms. For example, hydrogen atoms have a large incoherent scattering cross-section, leading to a large background signal.[55, 56] Deuteration can be used to decrease this. Additionally, neutrons can be scattered coherently to reveal phonon excitations.[55] When neutrons interact with crystalline solids, they can absorb or emit energy equal to a quantum of

phonon energy, $h\upsilon$ (h = Planck constant; υ = frequency), by oscillating about their equilibrium position in the lattice at a given frequency.[57, 58]

One feature of INS is the lack of a symmetry-based selection rule. Thus, all vibrational modes are expected with this single analytical technique.[56] Unlike IR and Raman spectroscopies which are based on photons (or electromagnetic irradiation), neutrons are scattered via the interactions with atomic nuclei or electrons. While there are both internal modes (change in center-of-mass) and external modes (lattice vibrations) for molecular crystals, INS techniques do not distinguish between the internal and external modes.[57, 58] Thus, they are both called phonons.

1.5. Phonon computations and simulations of INS spectra

Ab-initio calculations give phonon energies and their symmetries. Since INS give all phonons, the computed phonons may be compared with the INS spectra. Magnetic transitions in INS are those not provided by the phonon calculations. Thus, comparing the calculated phonon spectra and the experimental INS spectra would reveal the magnetic transitions, including the magnetoelastic coupling.[59, 60] Vienna Ab-initio Simulation Package (VASP) is a computer program used for materials modeling on the atomic scale.[61] It can be used to perform many types of computations such as calculating the electronic structure or modeling quantum-mechanical molecular dynamics. We have chosen to use VASP computations to calculate the phonon peaks for SMMs

while simulating the VISION spectra at 0 K. As an example, our group recently used *ab-initio* calculations to better understand the magnetoelastic coupling in **1-*d*$_4$** and **1-*d*$_{18}$**.[38]

1.6. Hirshfeld surface calculations

Understanding intermolecular interactions helps probe whether SMMs behave truly as individual molecules/magnets or the interactions among the molecules in the crystals of the compounds, *e.g.*, relaxation from magnetic excited states. Hirshfeld surface analysis is a newly developed method to study interactions of an individual molecule with its nearest neighbor molecules.[62-65] It is a simple approach of mapping void space in molecular crystals. A Hirshfeld surface is an isosurface calculated from the weight function $w(\boldsymbol{r})$ of the sum of spherical atom electron densities in Eq. 3:

$$w(\boldsymbol{r}) = \frac{\rho_{promolecule}(\boldsymbol{r})}{\rho_{procrystal}(\boldsymbol{r})} = \sum_{A \in molecule} \rho_A(\boldsymbol{r}) \; / \sum_{A \in crystal} \rho_A(\boldsymbol{r}) \qquad \text{(Eq. 2.3)}$$

where $\rho_{\text{promolecule}}(\boldsymbol{r})$ = sum of the molecular electron density over the atoms in the molecule of interest (the promolecule); $\rho_{\text{procrystal}}(\boldsymbol{r})$ = similar sum over the crystal (the procrystal).

The Hirshfeld surface leads to a visual 3-*D* representation of the intermolecular close contacts in the crystal and computations of surface areas

and volumes of the voids in the crystals.[66] Hirshfeld surface analysis is an excellent method to study molecular environment and interactions of compounds independent of the overall space group symmetry. We recently used the Hirshfeld surface analyses to study structures of metalloporphyrins Fe(TPP)Cl (TPP^{2-} = tetraphenyl porphyrinate),[67] M(TPP)(NO)[67] (M = Fe, Co) and Mn(TPP)X•solvent[68] (X = Br, solvent = $CHCl_3$, CH_2Cl_2; X = I, solvent = $CHCl_3$, $CDCl_3$ and $1.5CHCl_3$). These analyses show that intermolecular interactions contribute significantly to structural disorders of Fe(TPP)Cl and phase changes in M(TPP)(NO) (M = Fe, Co).[67]

1.7. Overview of the thesis

This thesis serves to explore the magnetic properties of three highly anisotropic molecules using spectroscopic studies and calculations.

The first compound, $[Ni(Me_6TREN)Cl]ClO_4$ (**2**), has been probed by FIRMS, Raman magnetospectroscopy, and Hirshfeld computations. Far-IR studies are used to directly observe the transition between ZFS states (*i.e.*, magnetic transition) and Hirshfeld surface analyses models intermolecular interactions in the crystal.

The second compound, $Dy(acac)_3(H_2O)_2$ (**3**), and its isotopologues $Dy(acac\text{-}d_7)_3(H_2O)_2$ (**3-*d*$_{21}$**) and $Dy(acac\text{-}d_7)_3(D_2O)_2$ (**3-*d*$_{25}$**), exhibit typical SMM behavior including spin-phonon coupling, as shown by FIRMS studies. Although no new information is gained, Raman magnetospectroscopic studies are

performed. INS studies can be used to confirm magnetic peaks. Furthermore, VASP computations can be applied to calculate a 0 K spectra which is comparable to the experimental data. This spectra was used to compute the symmetry of the phonons (irreducible representations). By looking at the deuterated isotopologues, we can observe the effect of deuteration on SMM behavior.

The third compound, Yb(trensal) (**4**), can act as both an SMM and qubit depending on the concentration. We use far-IR, Raman, and INS studies as well as VASP computations to look at the magnetic properties of **4** which should behave as an SMM.

CHAPTER 2. DIRECT DETERMINATION OF LARGE AXIAL ANISOTROPY IN A NICKEL(II) COMPLEX

This chapter is taken in part from the following publication:

Direct Observation of Magnetic Transitions in a Nickel(II) Complex with Large Anisotropy

Widener, C. N.; Bone, A. N.; Ozerov, M.; Richardson, R.; Lu, Z.; Thirunavukkuarasu, K.; Smirnov, D.; Chen, X.-T.; Xue, Z-L. *Chin. J. Inorg. Chem*. **2020**, *36*, 1149-1156. http://doi.org/10.11862/CJIC.2020.126

2.1. Abstract

Trigonal bipyramidal Ni(II) complex [Ni(Me_6tren)Cl](ClO_4) (**1**, Me_6tren = tris[2-(dimethylamino)ethyl]amine) has recently been shown by Ruamps and coworkers to possess large, uniaxial magnetic anisotropy.[69] Their HF-EPR studies gave rhombic ZFS parameter E = 1.56(5) cm^{-1} for **2**. However, the axial ZFS parameter D has not been determined. We have used FIRMS at 0-17.5 T and 5 K to probe the magnetic transitions between the $M_S = \pm 1$ and $M_S = 0$ states of the ground spin state S = 1 in **2**. Direct observation of the transitions between Zeeman-split states in FIRMS give axial ZFS parameter D = -110.7(3) cm^{-1}. Hirshfeld surface analysis of the crystal structure of **2** has been performed, revealing the interactions between the cation and anion in a molecule of **2** as well as among the molecules of **2** in crystals.

2.2. Introduction

Magnetic properties of transition metal complexes have been actively studied recently in part to understand the fundamental nature of the complexes and in part to probe their potential applications as SMMs and chemical qubits.[6-18, 20-23, 70, 71] For paramagnetic compounds with $S \geq 1$ and quenched orbital angular momenta, the ground electronic states of the compounds are split (ZFS) from second-order SOC involving the ground electronic states.[6-12, 14-18, 20, 22, 23, 70, 71] The degree of the magnetic anisotropy is measured by axial (D) and rhombic (E) ZFS parameters.[7] Ni(II) complexes displaying SMM

properties have been reported.[72-77] The d^8 complex in the current study, **2**, contains a trigonal bipyramidal cation (Figure 2.1). In the trigonal crystal structure of **2** (*R*3*c* space group, No. 161), the $[Ni(Me_6tren)Cl]^+$ cation sits on a 3-fold axis (Figure 2.1b). Thus, the crystallographic point group symmetry of the metal site (paramagnetic center) is axial and 3-fold. In other words, the *x*,*y* directions are degenerate. However, as discussed below, Jahn-Teller distortion leads to the breakup of the degeneracy.

The d orbitals in the Ni ion in **2** are split by the ligand field into three sets as shown in Figure 2.1-Right. There are three electrons in the middle level, a degenerate set (*e*). Jahn-Teller distortion of the molecule of **2** to lower the energy leads to the splitting of the degenerate orbitals, as shown in Figure 2.1-Right. With such five non-degenerate d orbitals in the Jahn-Teller distorted cation $[Ni(Me_6tren)Cl]^+$, the orbital angular momentum is quenched. The two unpaired electrons in the Ni(II) complex ($S = 1$) undergo second-order spin-orbital coupling with excited electronic states, leading to zero-field splitting (ZFS) of the triplet ground electronic state $^3A_2$ into the $M_S = 0$ and doublet $M_S = \pm 1$ states. When the axial parameter $D < 0$, as in **2**, the molecule has an easy axis of magnetization in the *z* direction (or uniaxial magnetic anisotropy) which is typically assumed to be parallel to the C_3 axis. When $D > 0$, the molecule possesses an easy plane of magnetization in the *x,y* direction. In the Jahn-Teller distorted $[Ni(Me_6tren)Cl]^+$, there is additional splitting of the degenerate $M_S = \pm 1$ states by the rhombic (*E*) parameter (Figure 2.2). The determination of the ZFS parameters is vital to

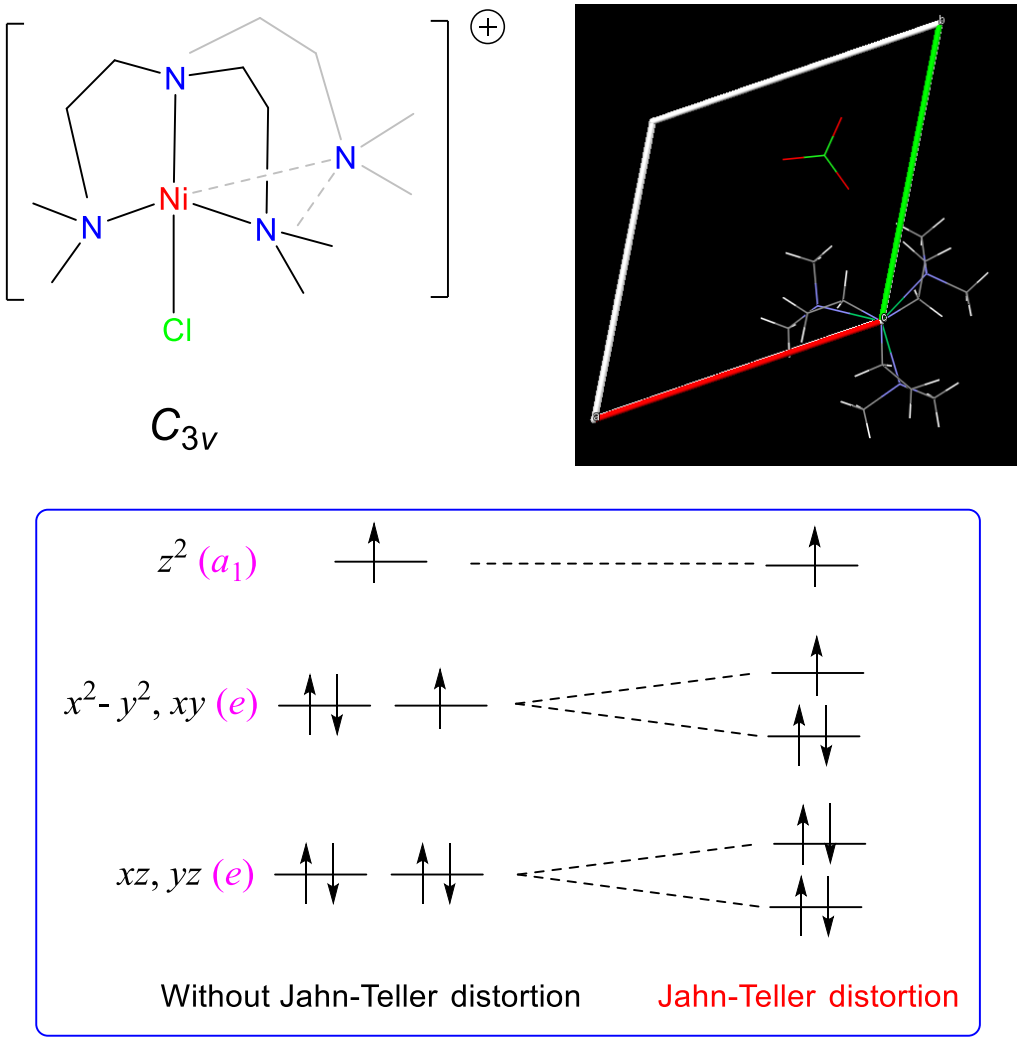

Figure 2.1. (Left) $[Ni(Me_6tren)Cl]^+$ cation in **2** with local C_{3v} symmetry. (Right) View of the cation and anion in **2** looking down the crystallographic *c* axis, showing that the cation is on a C_3 axis. *a* axis: red; *b* axis: green. (Bottom) Splitting of the d orbitals in the $[Ni(Me_6tren)Cl]^+$ cation. The a_1 and *e* symbols refer to the symmetries of the d orbitals in the C_{3v} point group.

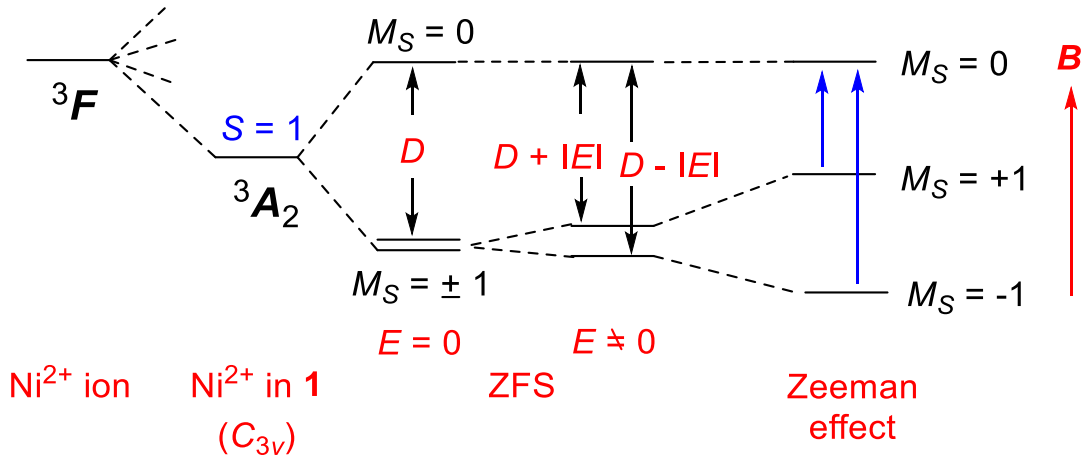

Figure 2.2. Ground-state triplet levels in high-spin, d^8 complexes with C_{3v} symmetry and uniaxial magnetic anisotropy ($D < 0$). $E \neq 0$ leads to additional splitting of the degenerate $M_S = \pm 1$ states. Under magnetic fields, the Zeeman effect shifts the $M_S = -1$ and $M_S = +1$ states. The $M_S = -1 \rightarrow 0$ and $M_S = +1 \rightarrow 0$ transitions at low temperatures are allowed.

understanding magnetic properties of the complex.[6-12, 14-18, 20, 22, 23, 70, 71]

Magnetometry (or direct-current magnetic measurements) is often employed to estimate the ZFS in metal complexes, even though this is an indirect method based on essentially a multi-parameter fit of susceptibility and magnetization data by the spin-Hamiltonian.[14] In addition, the sign of *D* is often not easily determined by magnetometry. HF-EPR has been used to study ZFS typically up to ~33 cm^{-1} (1 THz).[14, 25] Ruamps and coworkers have used HF-EPR to probe a single crystal of **2** to give E = 1.56(5) cm^{-1} and g_z = 2.34(7). The *D* value in **2** was estimated to be between -120 and -180 cm^{-1}.[69] A subsequent semiempirical model study of the Ni(II) ion in **2** has been conducted to analyze the large ZFS.[78]

In the current work, we have used FIRMS at 5 K to probe the ZFS transitions in **2**. By using E = 1.56 cm^{-1} from the earlier HF-EPR studies, simulating the far-IR data gives D = -110.7(3) cm^{-1}.[69] Hirshfeld surface analyses of the crystal structure of **2** show the interactions among the ions (cations $[Ni(Me_6tren)Cl]^+$ and anions ClO_4^-) in the crystalline solid of **2.**

2.3. Experimental

2.3.1. Synthesis

The ligand Me_6TREN was prepared by mixing tris(2-aminoethyl)amine (also known as TREN), formic acid, formaldehyde, and water at an elevated temperature. Then, complex **2** was synthesized according to the literature.[69]

Crystals were formed by slow cooling a hot saturated methanolic solution overnight.

2.3.2. Far-IR studies

Far-IR spectroscopic studies were conducted at the National High Magnetic Field Laboratory (NHMFL) at Florida State University. Transmittance far-IR spectra were collected using the powdered samples. The samples were mixed with eicosane and pressed into pellets that were approximately 1 mm thick. Spectra were collected at 5 K using a Bruker Vertex 80v FT-IR spectrometer coupled with a superconducting magnet (SCM 3) with fields up to 17.5 T.

2.3.3. Raman studies

Raman samples were prepared with unoriented single crystals of **2** (green crystal in Figure 2.3). Data were collected by a backscattering Faraday geometry using a 532 nm laser at an 18 T superconducting magnet (SCM 2) in the DC Field facility or at a 14 T SCM in the Electron Magnetic Resonance (EMR) facility. Crystals of samples were cooled at 4.5 K (18 T). Collected scattered light was guided via an optical fiber to a spectrometer equipped with a liquid nitrogen-cooled CCD camera.

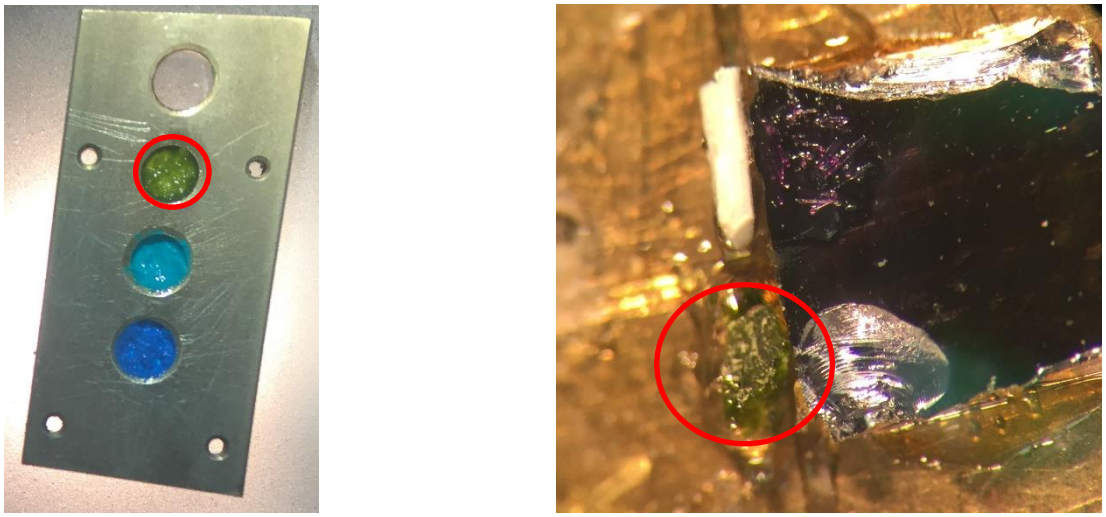

Figure 2.3. Photos of the samples of **2** for far-IR (Left) and Raman (Right) spectroscopic studies.

2.3.4. Hirshfeld surface calculation

Hirshfeld surfaces were calculated using CrystalExplorer (version 17) software from the crystal-structure coordinates supplied in the format of crystallographic information file (CIF).[79] The reported X-ray CIF file of **2** at 100(1) K (CCDC 893397) was used.[69] Hirshfeld surfaces were calculated at an isovalue of 0.5 e au^{-3}. Void volumes were calculated using an isovalue of 0.002 e au^{-3}.[66]

2.4. Results and discussion

2.4.1. FIRMS studies

The ZFS in the Ni compound was studied by FIRMS. This technique employs the Fourier-transform spectrometer to measure the magnetic response from the sample in the frequency domain (down to 20 cm^{-1}). The sample was placed in a cryostat equipped by a vertical bore superconducting magnet and coupled to the spectrometer through the evacuated optical beam line. In this manner, the intensity of far-IR radiation transmitted through the sample was recorded with magnetic fields (up to 17 T) and at temperature of 4.5 K. In all measurements, the magnetic field was applied in Voigt geometry (magnetic field perpendicular to the wave vector of the radiation). All samples were a mixture of the eicosane matrix with microcrystalline powders and different trials were made for a variety of mixture ratios and sample thicknesses. The FIRMS spectra and a contour plot of normalized transmission are shown in Figure 2.4. Transmission of

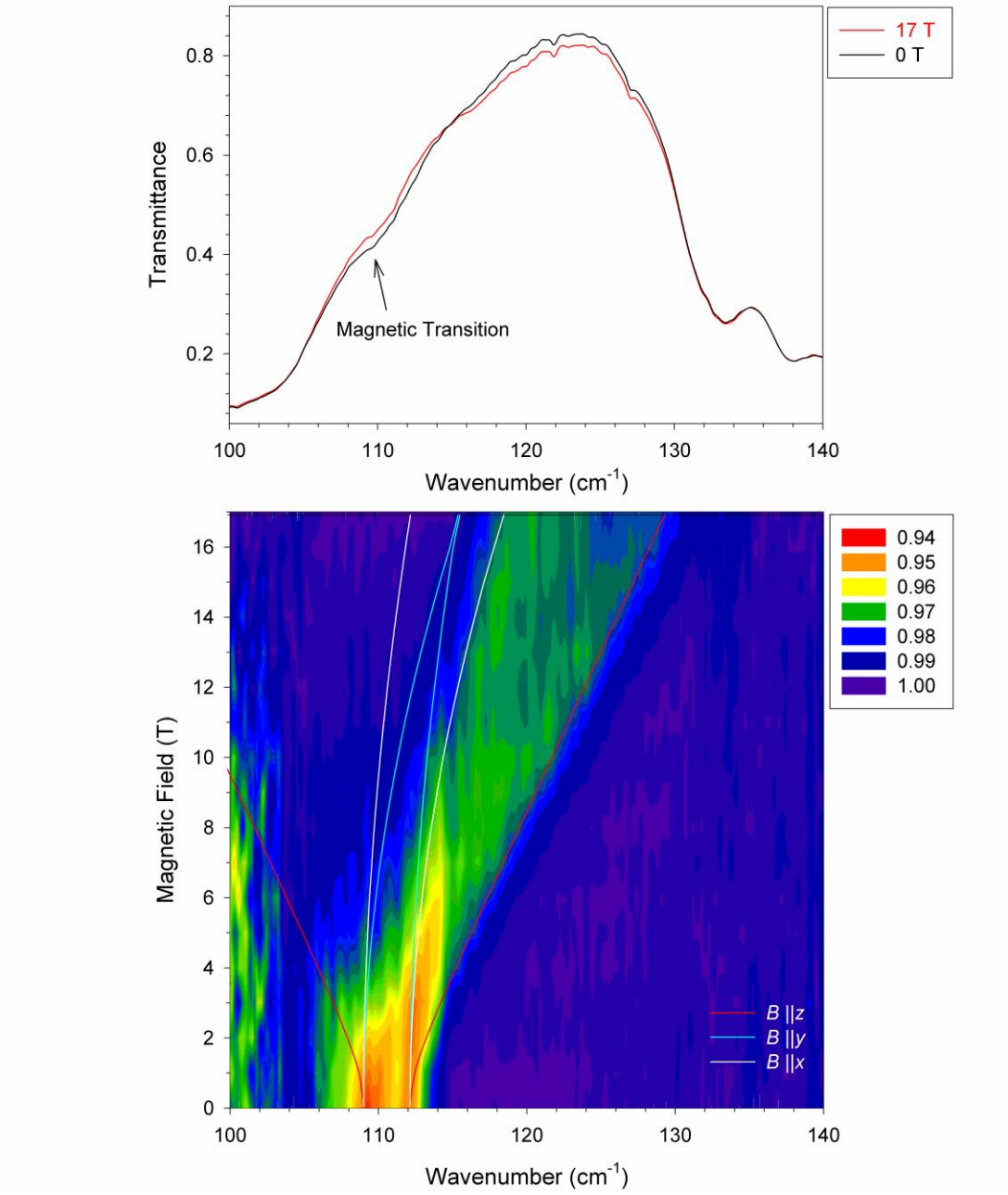

Figure 2.4. (Top) Far-IR spectra of **2** at 0 and 17 T magnetic fields. (Bottom) Contour map of normalized transmission in 0–17 T magnetic fields by the Filled Contour Plot in SigmaPlot 2000. Low-intensity regions indicate the presence of peaks. Simulations by the *EasySpin* program for the Zeeman splittings in the *B*||*x*, *B*||*y* and *B*||*z* directions are given.

2 normalized to the zero-field spectrum T_B/T_0 at 1-17 T is given in Figure A1 in Appendix.

For the interpretation of far-IR data of the Ni compound **2**, the measured data are presented in terms of normalized transmission. The transmission spectrum measured at each magnetic field was normalized to the reference spectrum computed as an averaging of spectra for all magnetic fields and removing outlier points. Such normalization reveals field-induced features masked at the original spectra due to the overlapping of the feature with phononic or intramolecular vibrational excitations. The quantitative contribution of magnetic excitations to absolute absorption of the sample is determined by the decrease in the normalized transmission. Therefore, this experimentally accessible quantity allows direct access to the transition intensity between field-dependent spin energy levels.

An in-house simulation program was written in Matlab for analysis of the magnetic field dependence of normalized transmission. The program is based on the *EasySpin* toolbox, allowing the calculations of the transition matrix element of the magnetic dipole transitions. Originally developed for the simulating and fitting a wide range of EPR spectra, the *EasySpin* toolbox provides frequency-domain simulation capabilities.[80] The simulation is performed for single magnetic center with the $S = 1$ spin Hamiltonian

$$\hat{H} = \mu_B \vec{B} \cdot \hat{g} \cdot \vec{S} + \vec{S} \cdot \hat{D} \cdot \vec{S} \qquad \text{(Eq. 2.1)}$$

where μ_B is Bohr magneton constant, $\vec{B}$ is magnetic field vector, $\vec{S}$ is vector spin operator, and $\hat{g} = \begin{pmatrix} g_x & 0 & 0 \\ 0 & g_y & 0 \\ 0 & 0 & g_z \end{pmatrix}$ is Landé tensors of the electron spin, and $\widehat{D} = \begin{pmatrix} -\frac{1}{3}D + E & 0 & 0 \\ 0 & -\frac{1}{3}D - E & 0 \\ 0 & 0 & -\frac{2}{3}D \end{pmatrix}$ is the ZFS tensor expressed by commonly used *D* and *E* zero-field splitting parameters. The input parameters $g_x = g_y = 2.4$, $g_z = 2.34$ and $E = 1.56$ cm^{-1} were fixed and taken from Ref. 69. *D* was only one variable parameter. The final absorption intensity spectra are obtained by introducing the line broadening parameter onto the calculated transition probabilities. The results of the simulation are shown in Figure 2.4-Bottom. The simulations yielded $D = -110.7(3)$ cm^{-1}.

2.4.2. Raman spectra

Raman spectra of a cut crystal of **2** show no discernible magnetic feature (Figure 2.5). The ZFS transition in the range of the magnetic feature in far-IR (Figure 2.4) was not observed in Raman spectra. Although the ZFS transition was not observed in Raman spectra of $Co(acac)_2(H_2O)_2$ (**1**, $acac^-$ = acetylacetonate), the spin-phonon coupling of the ZFS transition and nearby Raman-active phonons allow the ZFS transitions to obtain the intensities of the phonon transitions, leading to the observation of both ZFS and phonon peaks.[38]

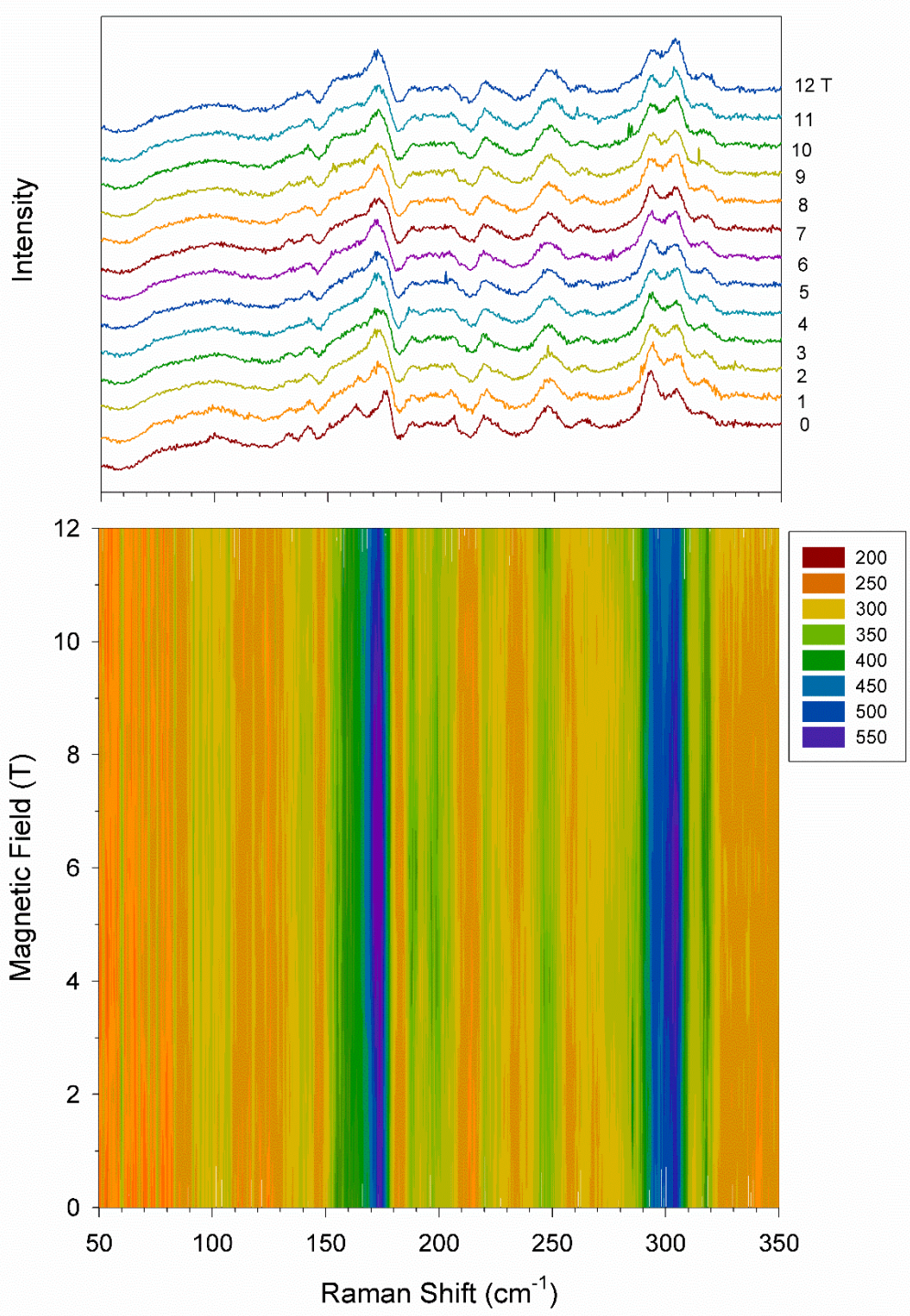

Figure 2.5. (Top) Raman spectra of **2** at 5 K and 0-12 T external magnetic fields. (Bottom) Contour plot of the Raman spectra at 0-12 T magnetic fields. Raman-active phonon peaks have higher intensity.

However, there is apparently no Raman-active phonons near the ZFS transition in the Ni(II) complex **2** here (Figure 2.5).

2.4.3. Hirshfeld surface analyses

Hirshfeld surface of **2** at 100(1) K is presented in Figure 2.6 with views from the top, bottom and side of the cation $[Ni(Me_6tren)Cl]^+$. Sites of close contacts are shown in red dots. Although there is close contact involving the "top" N atom on the C_3 axis, the void between two [2-(dimethylamino)ethyl]amine "arms" involves close contact with the anion ClO_4^-, as revealed in the top and side views in Figure 2.6. The bottom views (Figure 2.6) show that Cl^- ligand is in close contact with the H atoms of the methyl groups on the neighboring molecules. Additional views of the Hirshfeld surface with the packing diagram are given in Figures A2 and A3 in Appendix. The volumes and surface areas of the cation, anion ClO_4^- and the void in the crystal of **2** from the Hirshfeld surface analyses are given in Table 2.1.

Fingerprint plots, such as those in Figure 2.6 derived from the Hirshfeld surface, provide a "fingerprint" of the intermolecular interactions in the crystal of the compound.[62-66, 81] They give a visual summary of the frequency of d_e and d_i combinations across the surface of a molecule.[82] d_e is the distance from the surface to the nearest nucleus *external* to the surface. d_i is the distance from the surface to the nearest nucleus *internal* to the surface.[64, 83] Each point on the 2D graph (Figure 2.7) represents a bin of width 0.01 Å in d_e and d_i with color

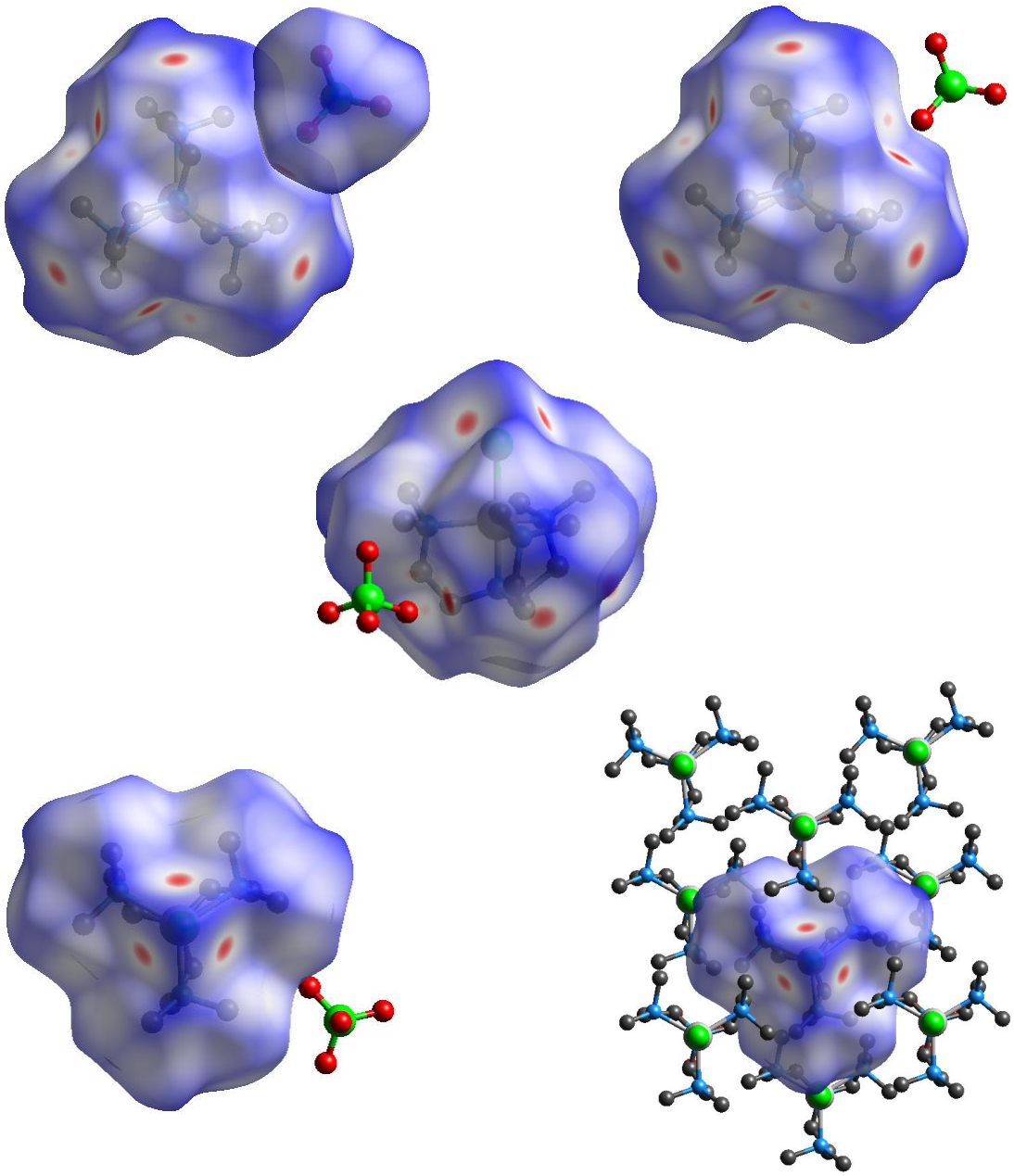

Figure 2.6. Hirshfeld surface of **2** showing normalized close distances of the pro-molecule at 100(1) K. Semi-transparent view reveals the enclosed cation and anion. (Top) Hirshfeld surface – Top views (Looking down the N-Ni bond); (Middle) Side view; (Bottom) Bottom views (Looking down the Cl-Ni bond) with a packing diagram.

Table 2.1. Volumes and surface areas in **2** from Hirshfeld surface analyses

	Volume (A^3)	Surface area (A^2)
$[Ni(Me_6tren)Cl]^+$ cation	382.57	294.87
ClO_4^- anion	71.77	90.57
Void	298.76	956.27

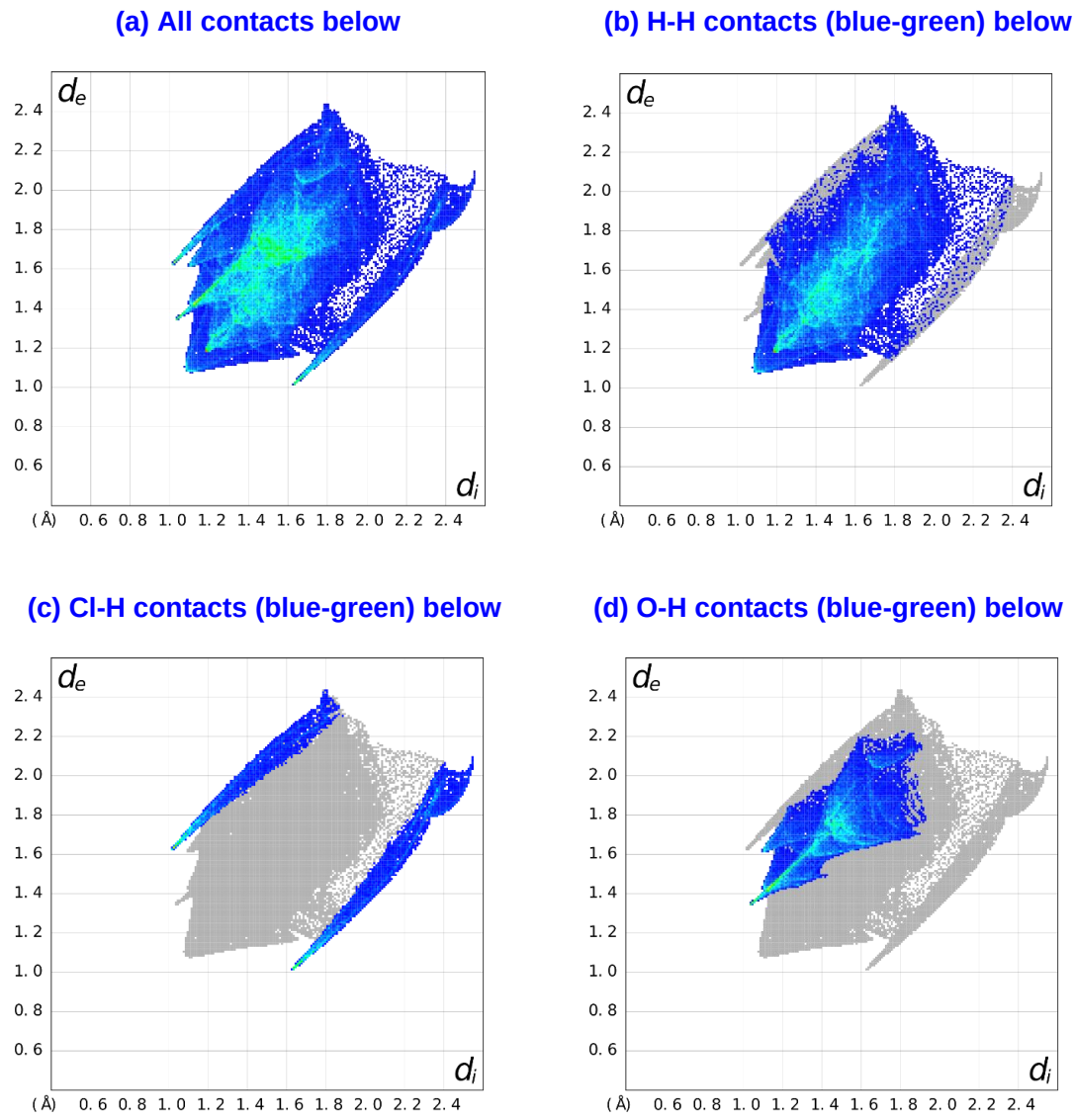

Figure 2.7. Hirshfeld fingerprint plots.

indicating the fraction of surface points in that bin: blue (relatively few points), green (moderate fraction) and red (many points).[64] As Spackman and coworkers indicated, the d_e and d_i range varies considerably across the Hirshfeld surface, and the change depends on the atoms in the molecule (*i.e.*, size dependence) and the type of intermolecular interaction involved (*i.e.*, interaction dependence).[84] Figure 2.7 shows that the closest contacts correspond to the minimum values of $d_e + d_i$ are: 2.2 Å for H···H (Figure 2.7b); 2.6 Å for Cl···H (Figure 2.7c); 2.4 Å for O···H (Figure 2.7d). The H···H contacts, as like···like contacts are featured more along the diagonal (Figure 2.7b).[85] The 'wings' in Figure 2.7a are due to the Cl···H (Figure 2.7c) and O···H interactions (Figure 2.7d).

At present, the links between the results of the Hirshfeld surface analyses and relaxation of **2** from its magnetic excited (ZFS) state are not clear. However, it is believed that the interactions between the cation and anion in **2** and between molecules of **2** are part of the phonons (*i.e.*, both intramolecular and intermolecular vibrational modes) in the solid of **2**. Through spin-phonon coupling, the interactions revealed by the Hirshfeld surface analyses may contribute to the magnetic relaxation.

2.5. Conclusions

In summary, the current work led to explicit observation of the transition between ZFS states in **2** by FIRMS, directly determining the axial ZFS parameter

D = -110.7(3) cm^{-1}. Thus, both ZFS parameters, D and the rhombic E = 1.56(5) cm^{-1} from earlier HF-EPR studies, are obtained, providing an excellent example of using combined spectroscopies to determine accurately the spin-Hamiltonian parameters in an SMM. Hirshfeld surface analyses of the crystal structure of **2** at 100(1) K give volumes and surface areas of the cation $[Ni(Me_6tren)Cl]^+$, anion ClO_4^- and void in **2**. In addition, “fingerprints” of the intermolecular interactions reveal the intermolecular interactions in the crystal.

CHAPTER 3. SPECTROSCOPIC PROPERTIES OF A DYSPROSIUM(III) SINGLE-MOLECULE MAGNET COMPLEX

3.1. Abstract

$Dy(acac)_3(H_2O)_2$ (**3**) is a Dy(III) complex with approximately D_{4d} symmetry (based upon Dy-O bonds).[86] The energy separation, 27.8 cm^{-1}, between the ground state (M_J = ±13/2) and first excited state (M_J = ±11/2) has been determined by Jiang using susceptibility studies and computations.[86] We have perform FIRMS studies to observe magnetic peaks, phonon peaks, and the interactions between the two (spin-phonon coupling). Deuterating the complex results in slightly lower energy peaks. Far-IR spectra of crystals show the behavior of the magnetic peaks more clearly than far-IR spectra of powders when there are multiple phonons close together. Furthermore, Raman magnetospectroscopy is used to identify phonons not found in far-IR as well as confirm the presence of magnetic hysteresis, a key feature of SMMs. Finally, INS and VASP computations are used to identify all magnetic and phonon peaks in the complete neutron scattering range and determine their symmetries.

3.2. Introduction

The Dy(III) ion has a $4f^9$ spin-orbit coupled ground state. The strong orbital contribution to the magnetic moment results in a $^6H_{15/2}$ collection of states (where S = 5/2; L = 5; J = 15/2).[19] This is important because the SOC is typically much stronger than the splitting of the crystal field for complexes of lanthanides and actinides as shown in Figure 1.3. The ground state is 16-fold degenerate with M_J = ±15/2, ±13/2, ±11/2, ±9/2, ±7/2, ±5/2, ±3/2, and ±1/2 KDs. This creates a

relatively large spin barrier to relaxation, as the magnetic relaxation would need to take the electrons from the M_J = +15/2 state to the M_J = +1/2 state in increments of 1 before descending to the M_J = -15/2 state. Therefore, higher degeneracy allows for a higher energy barrier. However, mixing of the states may lead to QTM, allowing the molecule to crossover from the +M_J state to the -M_J state (For example, M_J = +5/2 to M_J = -5/2 in Figure 3.1)

The Dy(III) ion has a strongly oblate spheroid electron density (Figure 1.3) which causes Dy(III) complexes to have an almost unparalleled magnetic anisotropy. Environments that consist of a strong axial crystal field and a weak equatorial crystal field, such as in **3**, further enhance the anisotropy of the Dy(III) ion in the complexes. Furthermore, the Dy(III) ion is described by Kramers theorem. In a complex with at least 3-fold symmetry on the metal ion that contains an odd number of electrons (and thus a half-integer total spin), its energy levels are at least doubly degenerate. Therefore, the molecule will display magnetic bistability as required for SMMs.

3 (Figure 3.2) has approximately D_{4d} symmetry (based upon Dy-O bonds).[87] X-ray diffraction study reveals **3** has a monoclinic crystal structure ($P2_1/n$ space group, No. 14). AC magnetic susceptibility measurements of **3** revealed a U_{eff} of 45.9 cm^{-1}.[87] The energy of the magnetic transition, *i.e.*, the excited state, is not given for the complex. Instead, the energy separation (E = 27.8 cm^{-1}) between the ground state (M_J = ±13/2) and first excited state (M_J = ±11/2) has been determined via DC magnetic susceptibility.

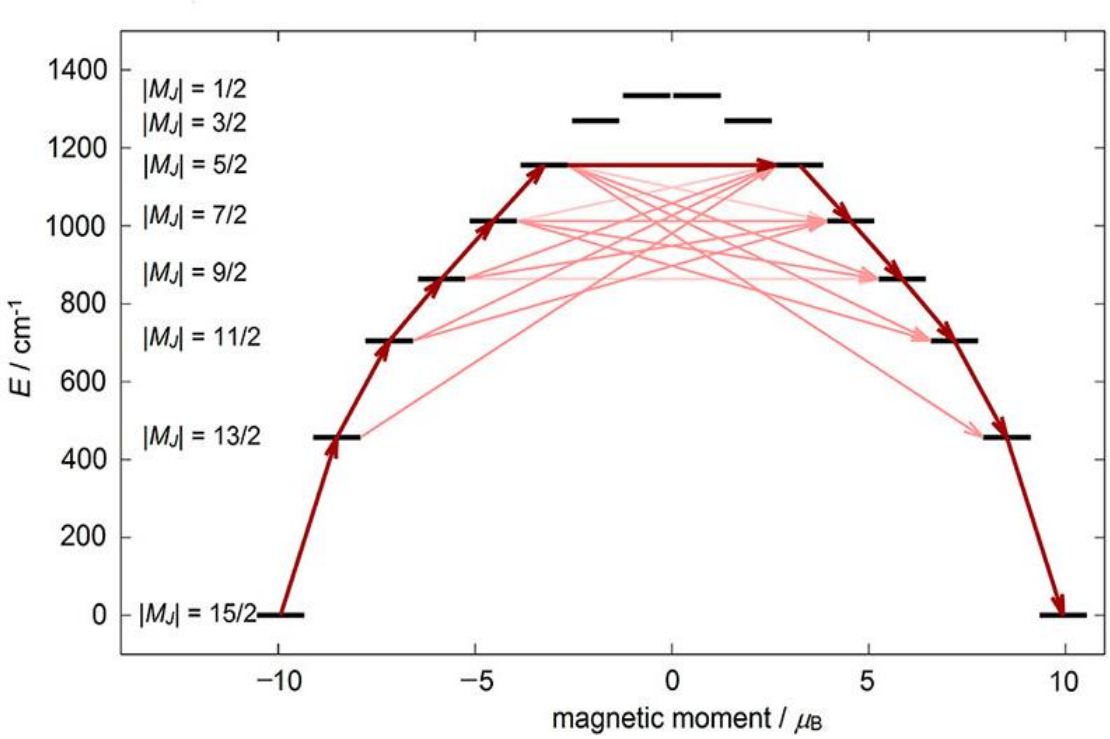

Figure 3.1. Relaxation pathways derived from ab-initio calculations of a fused-ring Dy(III) SMM where darker lines mean larger contribution to the overall relaxation. Reprinted with permission from Ref. 31. Copyright 2018 American Chemical Society.

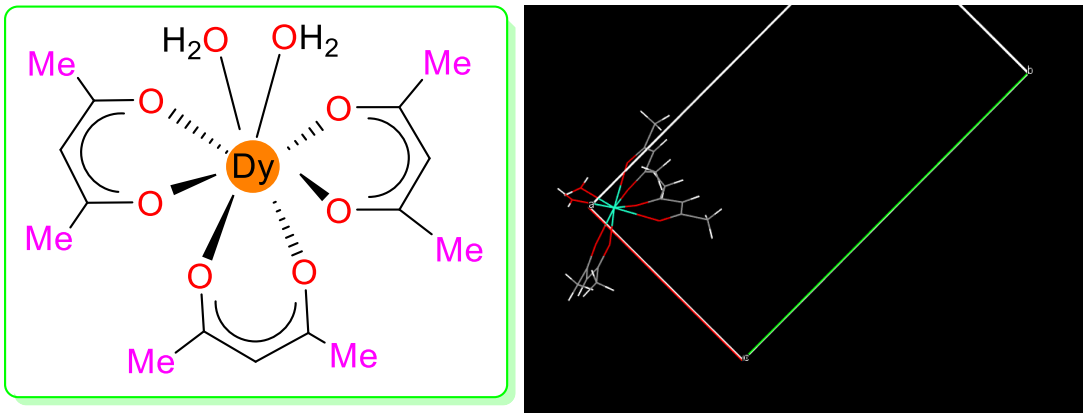

Figure 3.2. $Dy(acac)_3(H_2O)_2$ (**3**). (Left) Structure and (Right) View of **3** looking down the crystallographic *c* axis.

3.3. Experimental

3.3.1. Synthesis

Complex **3** was prepared according to the literature procedure.[88]

Deuterated acetylacetone was prepared by the method of Frediani *et al*.[89] The deuteration level (ranging from 89 to 96%) was determined for each synthesis batch using mass spectrometry.

Partially and fully deuterated isotopologues, $Dy(acac)_3(D_2O)_2$ (**3-*d*$_4$**), $Dy(acac\text{-}d_7)_3(H_2O)_2$ (**3-*d*$_{21}$**) and $Dy(acac\text{-}d_7)_3(D_2O)_2$ (**3-*d*$_{25}$**), have been prepared, by an analogous process, using D-acac-d_7 and/or D_2O[89] in place of Hacac and/or H_2O. In order to form **3-*d*$_4$** and **3-*d*$_{25}$**, EtOD was used as a solvent rather than EtOH to prevent an H/D exchange between D_2O and EtOH. Additionally, the deuterated reactions should be performed in a water-free (N_2) environment in order to prevent H-exchange with water in the air, especially for **3-*d*$_{21}$** and **3-*d*$_{25}$**.

3.3.2. FIRMS studies

Far-IR studies of **3** and its deuterated isotopologues, **3-*d*$_4$** and **3-*d*$_{25}$**, were performed in SCM 3 at NHMFL with variable magnetic fields (0-17.5 T) at 5 K. Transmittance spectra of the fully deuterated sample, **3-*d*$_{25}$**, were obtained by barely covering bottom of the sample well with a powdered sample and then adding eicosane on top (Figure 3.3). Instrument parameters were set to default except for the frequency of 7.5 KHz and 2 consecutive 3 min spectra were

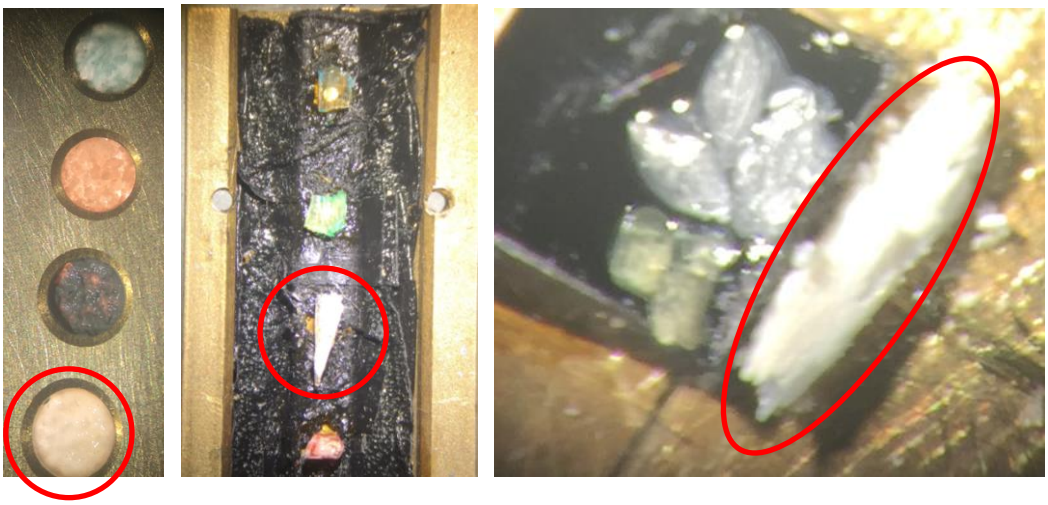

Figure 3.3. Photos of the samples of **3** for (Left) powder far-IR, (Middle) single-crystal far-IR, and (Right) Raman spectroscopic studies.

collected at different magnetic fields in 1 T increments from 0 to 17 T. The fully protonated sample, **3**, was run as a single crystal affixed to the sample well. The partially deuterated sample, **3-*d*$_4$**, was run as a single crystal at fields of 0 to 17.5 T in 0.5 T steps. All instrument parameters were kept consistent between the studies.

3.3.3. Raman studies

Raman samples were prepared with unoriented single crystals of **3**. Data was collected by a backscattering Faraday geometry using a 532 nm laser at SCM 2 (18 T) in the DC Field facility at NHMFL. Crystals of samples (Figure 3.3) were cooled at 4.5 K. Collected scattered light was guided via an optical fiber to a spectrometer equipped with a liquid nitrogen-cooled CCD camera.

3.3.4. INS study and phonon computations

Variable-temperature (VT) INS measurements at 5-150 K were taken on the VISION beam in the Spallation Neutron Source (SNS) at ORNL.

The crystal-structure information from the CIF file was loaded into VASP and used to generate the input file of phonon frequencies and polarization vectors (also gives irreducible representations). Then, OCLIMAX calculated VISION parameters (generates 0 K spectra). The reported X-ray CIF file of **3** at 100(1) K (CCDC 770557) was used.[88]

3.4. Results and discussion

3.4.1. FIRMS studies

In collecting far-IR spectra of **3** and its deuterated isotopologues inside magnetic fields, the samples were placed in a cryostat equipped by a vertical bore SCM and coupled to the spectrometer through the evacuated optical beam line. In this manner, the intensity of far-IR radiation transmitted through the sample was recorded with magnetic fields (up to 17 or 17.5 T) and at temperature of 4.5 K. In all measurements, the magnetic field is applied in Voigt geometry (magnetic field perpendicular to the wave vector of the radiation). All samples were a mixture of the eicosane matrix with microcrystalline powders or single crystal samples and different trials were made for a variety of deuterated compounds. The FIRMS spectra of **3**, **3-*d*$_4$**, and **3-*d*$_{25}$**, transmittance normalized to the zero-field spectra, and a contour plot are shown in Figures 3.4, 3.5, and 3.6, respectively. **3-*d*$_{21}$** needs to be re-run because too much sample was used resulting in complete absorbance of the incident phonons in some regions.

For the interpretation of far-IR data of the Dy(III) compounds, the measured data are presented in terms of normalized transmission. The transmission spectrum at each magnetic field was normalized to the reference spectrum computed as an averaging of spectra for all magnetic fields and removing outlier points. Such normalization shows up field-induced features that might be masked at the original spectra due to overlap with phononic excitations. The quantitative contribution of magnetic excitations to absolute absorption of the

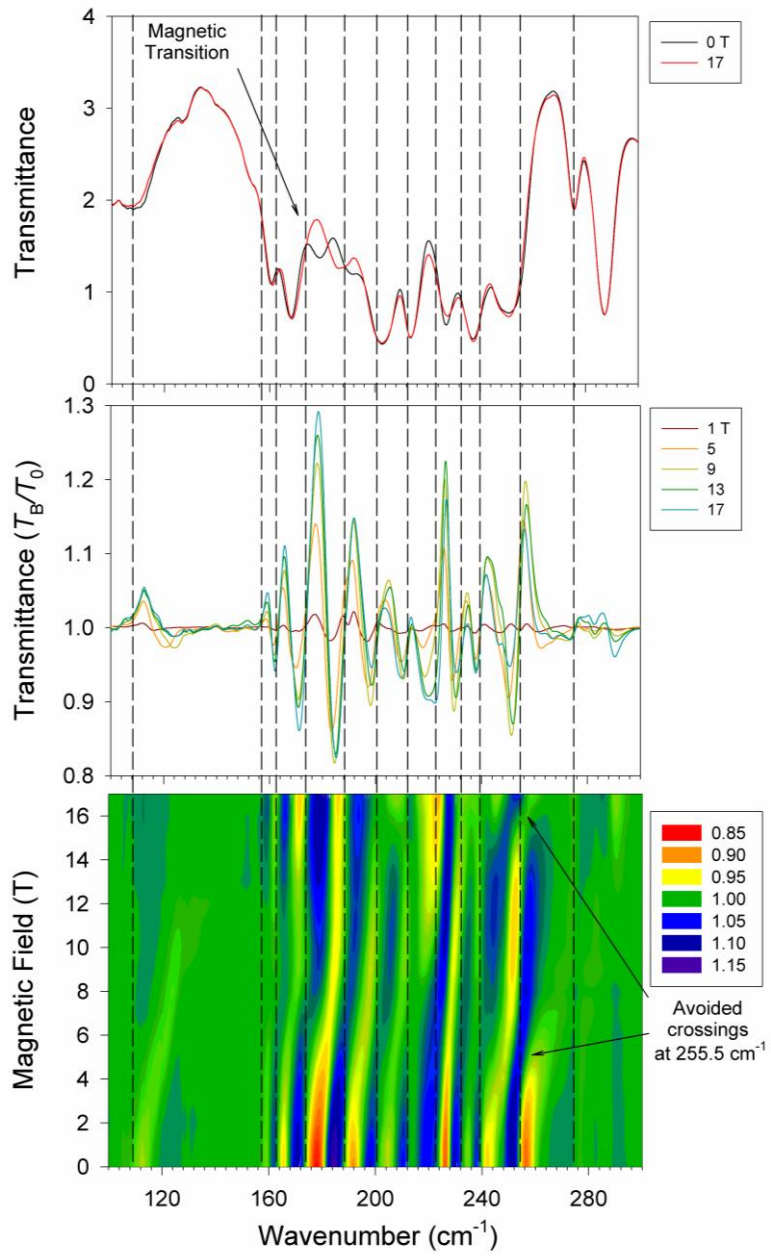

Figure 3.4. (Top) Far-IR spectra of **3** at 0 and 17 T magnetic fields. (Middle) Transmission normalized to the zero-field spectrum T_B/T_0 at 1-17 T. (Bottom) Contour map of normalized transmission in 0-17 T magnetic fields by the Filled Contour Plot in SigmaPlot 2000. Low-intensity regions indicate the presence of peaks. Each black dotted line indicates the location of a potential phonon.

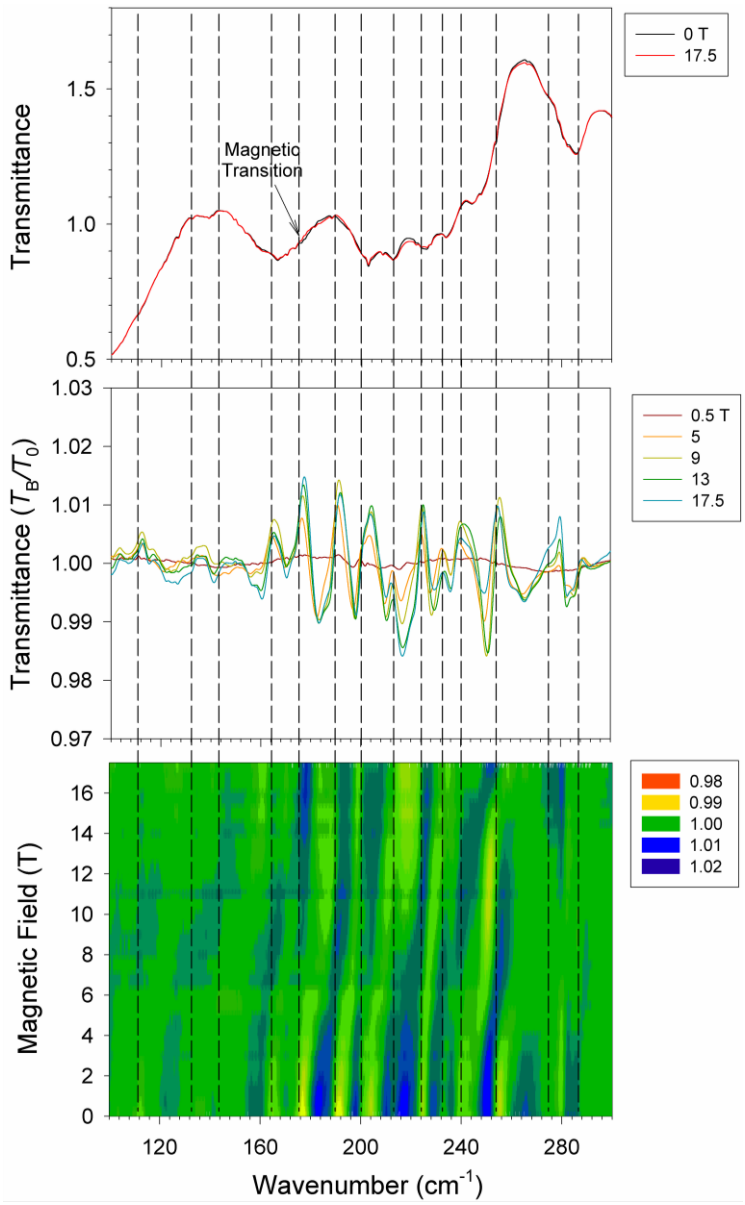

Figure 3.5. (Top) Far-IR spectra of a single crystal of **3-*d*$_4$** at 0 and 17.5 T magnetic fields. (Middle) Transmission normalized to the zero-field spectrum T_B/T_0 at 1-17 T. (Bottom) Contour map of normalized transmission in 0-17 T magnetic fields by the Filled Contour Plot in SigmaPlot 2000. Low-intensity regions indicate the presence of peaks. Each black dotted line indicates the location of a potential phonon.

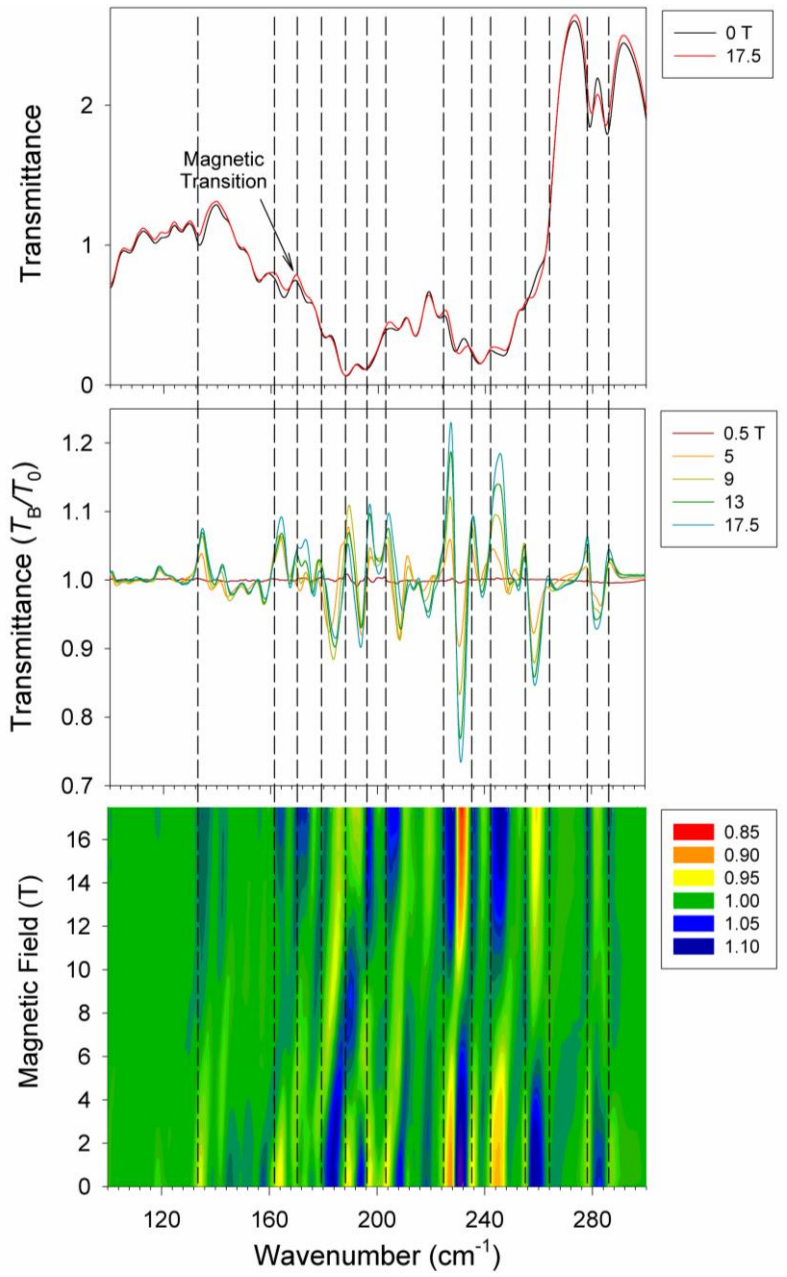

Figure 3.6. (Top) Far-IR spectra of **3-*d*$_{25}$** at 0 and 17 T magnetic fields. (Middle) Transmission normalized to the zero-field spectrum T_B/T_0 at 1-17 T. (Bottom) Contour map of normalized transmission in 0-17 T magnetic fields by the Filled Contour Plot in SigmaPlot 2000. Low-intensity regions indicate the presence of peaks. Each black dotted line indicates the location of a potential phonon.

sample is determined by the decrease in the normalized transmission. Therefore, this experimentally accessible quantity allows direct access to the transition intensity between field-dependent spin energy levels.

There is clear indication of a magnetic peak at 175.5 cm^{-1} in the spectra of **3**. Furthermore, the contour plot (Figure 3.4) shows evidence of multiple phonon peaks (164.5, 190.0, 202.0, 224.0, 240.5, and 255.5 cm^{-1}). Additional peaks found in the normalized transmittance spectra include 111.0, 159.0, 213.5, 233.5, and 275.5 cm^{-1}. Each phonon peak couples with at least one magnetic peak (spin-phonon coupling). As the magnetic field is increased, the frequency of the magnetic peak shifts. When it is close to a phonon with similar character, the two repel one another. This causes the magnetic peak to take on the characteristic of the phonon peak and vice versa. This is called an avoided crossing. We can infer the presence of multiple magnetic peaks from the presence of more than one avoided crossing at a single frequency as occurs at 255.5 cm^{-1}. Due to the proximity between the magnetic peaks and the numerous phonon peaks, it is not possible to accurately model the spin-phonon coupling at this time.

FIRMS spectra of complex **3-*d*$_4$** (Figure 3.5) are similar to those of **3**, but the changes as the magnetic field is increased are much less pronounced. Disregarding the difference in intensity, the contour plot of the **3-*d*$_4$** FIRMS data normalized by average is almost identical to that of **3**. The biggest difference between the two complexes is that the magnetic peak and the identified phonons have slightly different energies. The magnetic peak only shifts by 0.5 cm^{-1}.

Similarly, the phonons identified in the contour plot of **3** (Figure 3.4) are shifted 0.5-2.0 cm^{-1} to lower frequencies of 164.0, 189.5, 200.0, 240.0, and 254.0 cm^{-1}, respectively. Only the phonon at 224.0 cm^{-1} does not shift. The normalized transmission spectra are also similar with the additional peaks at 213.5, 164.5, and 190.0 cm^{-1} remaining unchanged while those at 111.0, 213.5, 233.5, and 275.5 cm^{-1} are shifted to lower frequencies of 110.5, 213.0, 232.5, and 275.0 cm^{-1}, respectively. Therefore, it seems that certain readily identifiable peaks in the partially deuterated (**3-*d*$_4$**) compound are slightly shifted to lower frequencies. Additionally, due to the smaller incoherent scattering D (as opposed to H), the noise levels will be lower, allowing additional features such as the potential peaks at 132.0, 143.0, and 287.0 cm^{-1} in the normalized transmission spectra. These replace the peak at 159.0 cm^{-1} in Figure 3.4.

FIRMS spectra of complex **3-*d*$_{25}$** (Figure 3.6) share many similar features with those of **3** and **3-*d*$_4$**. While possible phonons (133.0, 161.5, 170.0, 179.0, 188.0, 196.0, 203.0, 224.5, 235.0, 242.0, 255.0, 264.0, 278.0, and 286.0 cm^{-1}) can be found by comparing the spectra, normalized transmission, and normalized contour, the magnetic changes such as the v-shaped shifting of the two peaks around 200 cm^{-1} make the phonon peaks and spin-phonon coupling behavior harder to identify. This is because each magnetic peak has 3 possible shifting patterns (based upon if the magnetic field is along the *x*, *y*, or *z* axis). When a single crystal is used, the crystal is in one orientation. However, all orientations are mixed in the powder sample. As such, the FIRMS spectra of **3-**

***d*$_{25}$** cannot be compared with those of **3** or **3-*d*$_4$** unless an additional study is performed on a crystalline sample of **3-*d*$_{25}$** at a later date.

*3.4.2. Raman magnetospectroscopic studies of **3** and **3-*d*$_{25}$***

We have studied Raman magnetospectra of **3** and **3-*d*$_{25}$**, but no magnetic feature was observed. For **3**, even fields were collected with increasing magnetic field and odd fields were collected while decreasing the magnetic field (Figure 3.7). The difference in spectra is most likely due to magnetic hysteresis (retention of magnetic field) as the field is decreased.

There is a possibility of a coupling with the Raman-active phonon peaks, causing the Raman-inactive magnetic peak to gain the phonon features and showing up in the Raman spectra, as in the Raman spectra of $Co(acac)_2(H_2O)_2$ (**1**).[38] However, in this case, there is no evidence of such coupling despite the presence of multiple phonon peaks in the applicable range (near 175.5 cm^{-1} according to the far-IR spectra). **3-*d*$_{25}$** has similar Raman spectra to those of **3** except the field was increased (never decreased) from 0-17 T during the experiment (Figure 3.8).

3.4.3. INS study and phonon computations

VT-INS studies using powder samples of **3** were performed at VISION. The Bose-corrected forward scattering spectra are shown in Figure 3.9. There is

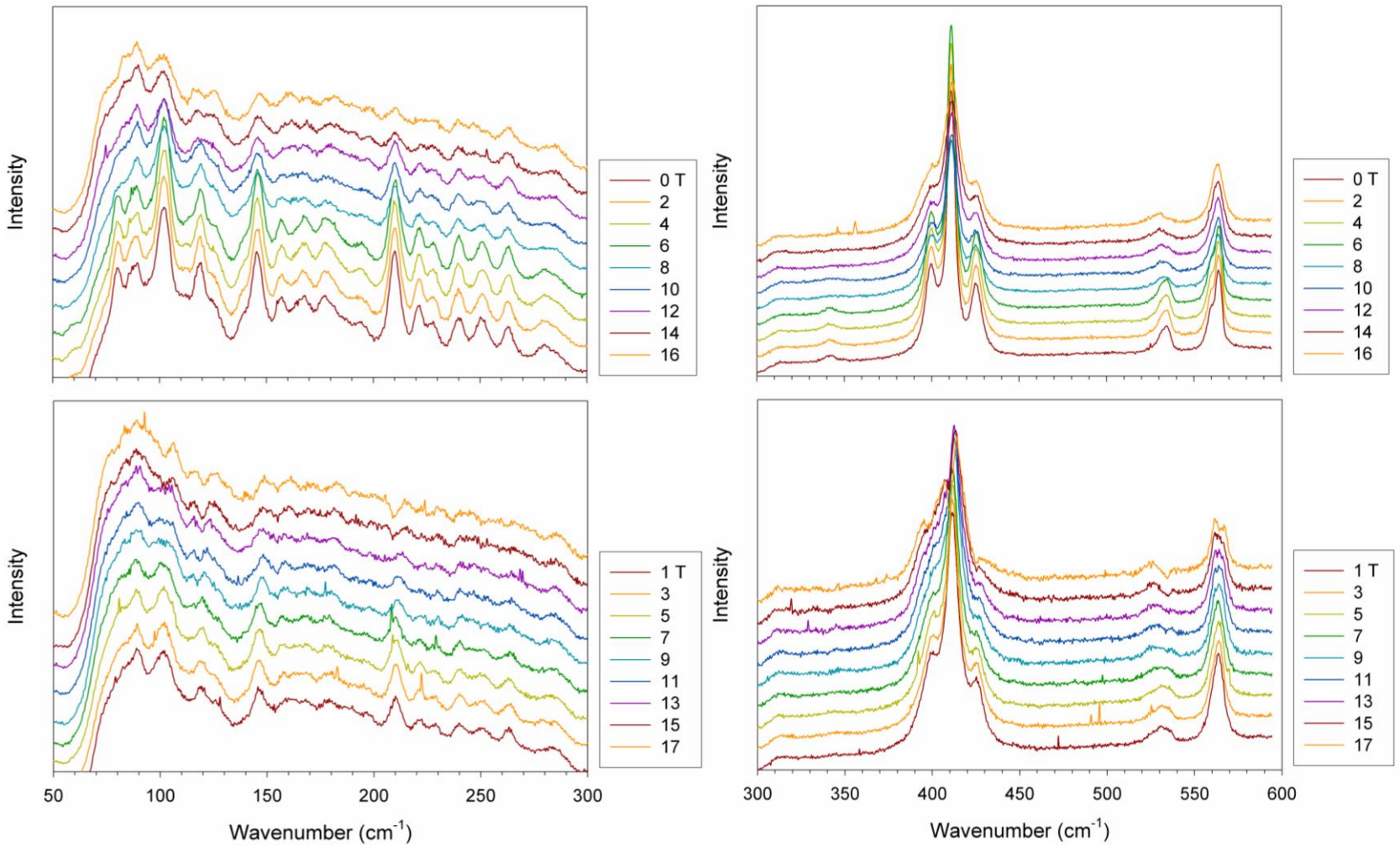

Figure 3.7. Raman spectra of **3** at 4.5 K and 0-17 T external magnetic fields. (Top) even fields; (Bottom) odd fields.

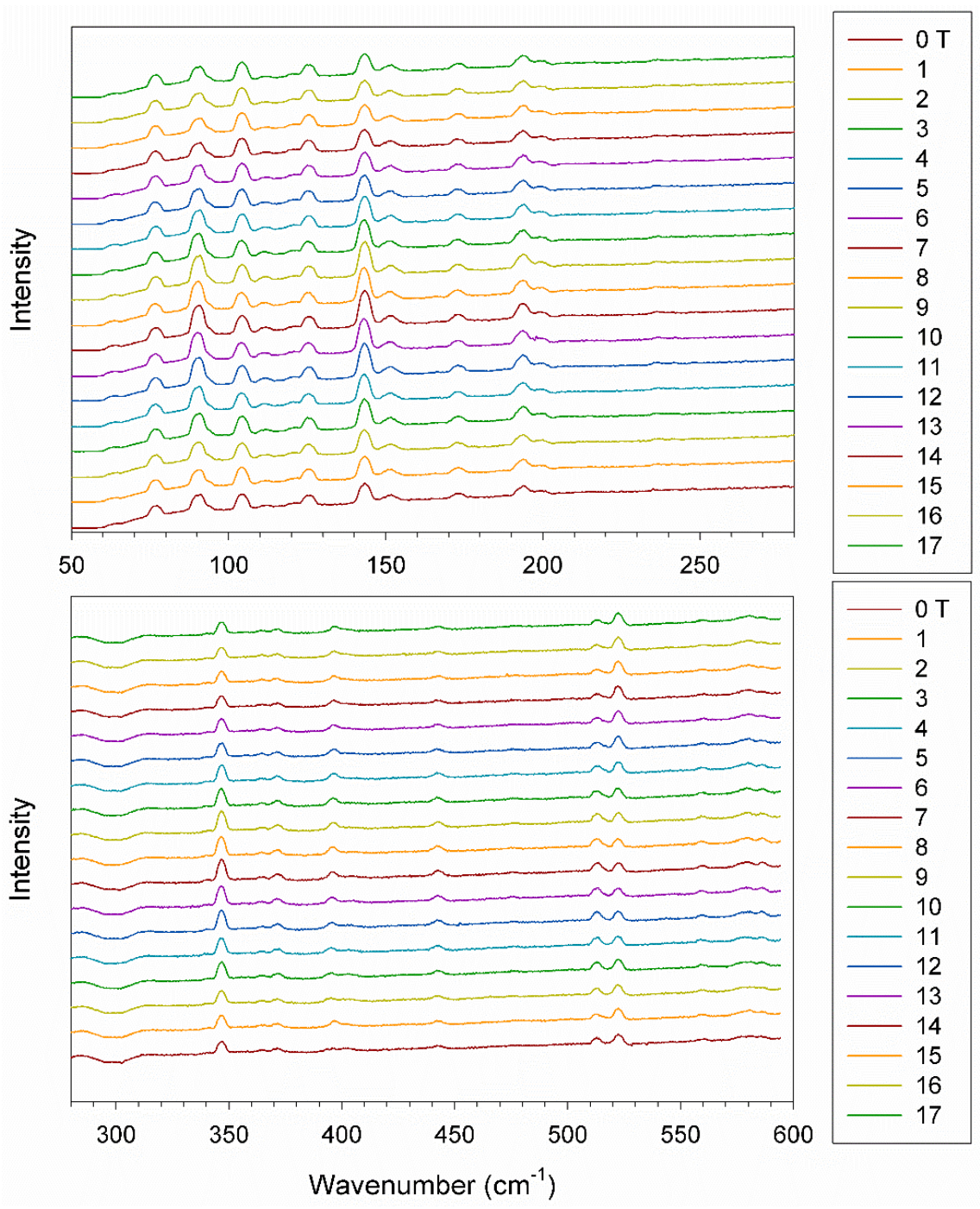

Figure 3.8. Raman spectra of **3-*d*$_{25}$** at 4.5 K and 0-17 T external magnetic fields.

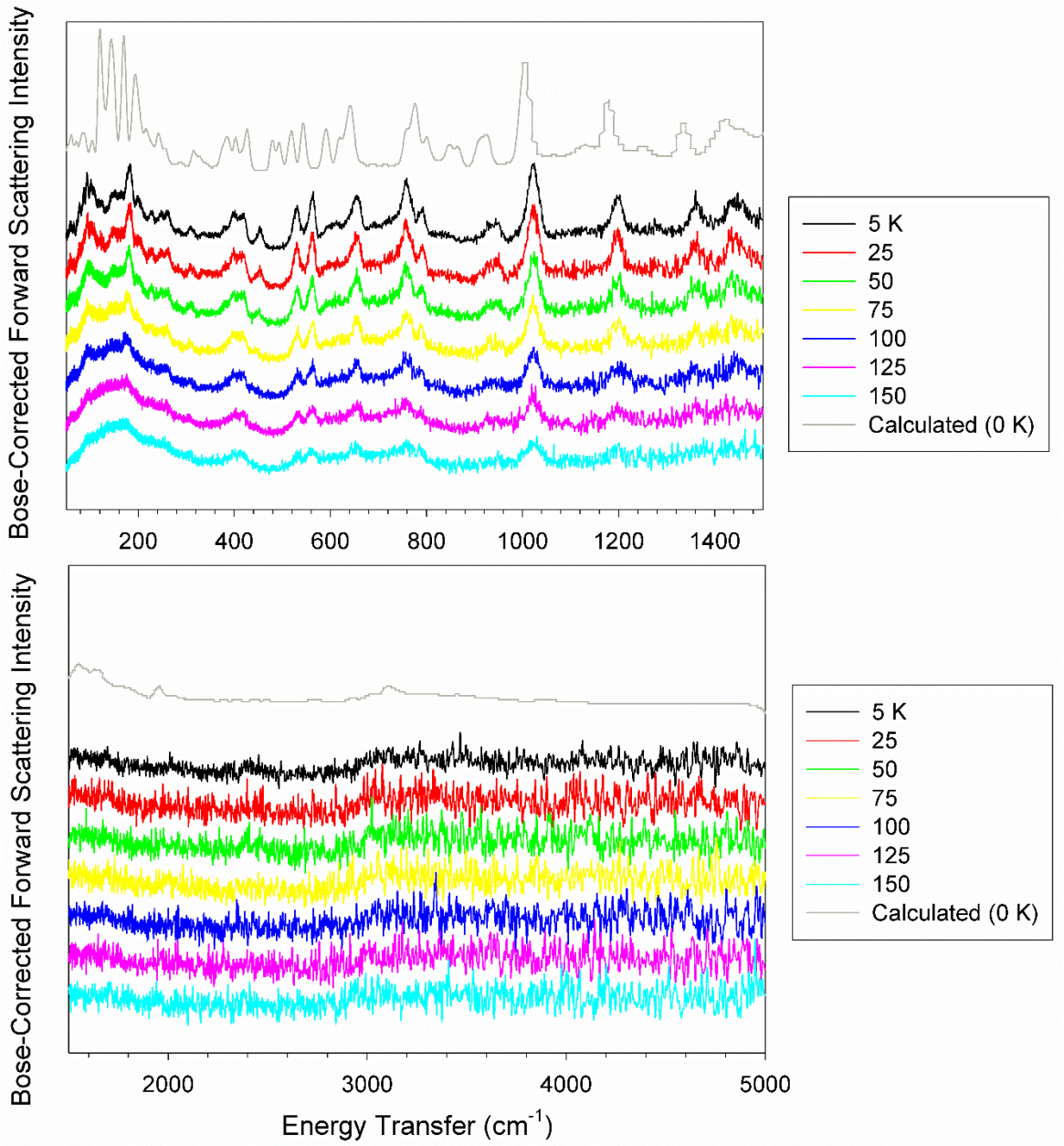

Figure 3.9. INS spectra of **3** at 5, 25, 50, 75, 100, 125 and 150 K on VISION. Calculated INS spectrum by VASP is shown in grey for comparison.

evidence of the same magnetic peak identified using far-IR in the INS spectra (175.5 cm^{-1}). However, it is not possible to identify this peak using INS alone due to the rapid decrease in intensity of multiple peaks as temperature is increased. However, this may also be due to the presence of multiple magnetic peaks as some peaks decrease faster than others.

VASP calculations resulted in a calculated (0 K) spectrum that match well with collected data, except at low frequencies where the agreement is poor. The symmetry analysis went well and each phonon was assigned an irreducible representation based upon the C_{2h} symmetry of the crystal. Based upon the forward scattering (FS) and back scattering (BS) intensities of the phonon peaks, we were able to determine the prevalent phonons in the region on interest (100-300 cm^{-1}). These phonons are modeled using Jmol (Animations 1-8).[90] Their intensities and symmetries are given in Table 3.1.

3.5. Conclusions

In summary, the current work led to direct observation of a magnetic transition in **3** (175.5 cm^{-1}) as well as other transitions perhaps between various M_J states. The utility of FIRMS studies using single-crystal samples (rather than powder) to get a clearer picture was demonstrated. Furthermore, it is likely that deuteration may slightly lower the energy gap between states although further studies are needed to confirm this observation.

Table 3.1. Animated phonons in $Dy(acac)_3(H_2O)_2$ (**3**) from VASP calculations

Frequency (cm^{-1})	BS Intensity	FS Intensity	Symmetry	Animation File
104.68	0.894(6)	0.415(8)	A_u	1_Complex 3_104.69_Au.mp4
121.97	2.358(9)	1.246(4)	A_u	2_Complex 3_121.97_Au.mp4
143.79	1.706(5)	0.973(2)	A_g	3_Complex 3_143.79_Ag.mp4
169.21	1.354(7)	0.911(3)	B_g	4_Complex 3_169.21_Bg.mp4
194.96	1.707(1)	1.066(6)	B_u	5_Complex 3_194.98_Bu.mp4
221.53	0.644(8)	0.424(9)	B_g	6_Complex 3_221.53_Bg.mp4
241.14	0.491(8)	0.322(4)	B_g	7_Complex 3_241.14_Bg.mp4
255.82	0.452(9)	0.297(5)	A_u	8_Complex 3_255.82_Au.mp4

CHAPTER 4. SPECTROSCOPIC PROPERTIES OF A YTTERBIUM(III) SINGLE-MOLECULE MAGNET COMPLEX

4.1. Abstract

Trigonal pyramidal Yb(III) complex Yb(trensal) (**4,** H_3trensal = 2,2',2"-tris(salicylideneimino)trimethylamine) has recently been shown by Pederson and coworkers to exhibit single molecule magnet behavior through DC and AC susceptibility measurements. Luminescence spectroscopy revealed the first excited electronic doublet at 454 cm^{-1}.[91] We have used FIRMS) at 0-17.5 T and 5 K to probe the magnetic behavior of IR-active peaks, revealing a repetitive pattern. INS and VASP computations reveal the phonons in the full neutron scattering range as well as the symmetry of many modes.

4.2. Introduction

Yb(trensal) (**4**) is a 7-coordinate, S = 1/2 complex with C_{3v} local symmetry (Figure 4.1-Left).[91, 92] **4** was reported by Costes and coworkers in 1999.[93] In their synthesis of **4**, the ligand precursor H_3trensal was prepared first before its reaction with $Yb(NO_3)_3 \cdot 6H_2O$ to give Yb(trensal)$\cdot H_2O$ in 82% yield. Bernhardt and coworkers synthesized **4** by a different approach – Direct reaction of $Yb(NO_3)_3 \cdot 6H_2O$ with salicylaldehyde and tris(2-aminoethyl)amine (TREN amine) without prior synthesis of H_3trensal and reported the work in 2001.[92] Here, the Yb(III) ion acts as a template in forming **4**. Bernhardt and coworkers determined the crystal structure of Yb(trensal) (**4**) at 296 K, showing that it has the trigonal space group *P*-3*c*1 (No. 165).[92] They also studied x-ray photoelectron spectroscopy of the complex, giving the binding energy of its 4d electrons at 185.4 eV.[94] Pedersen

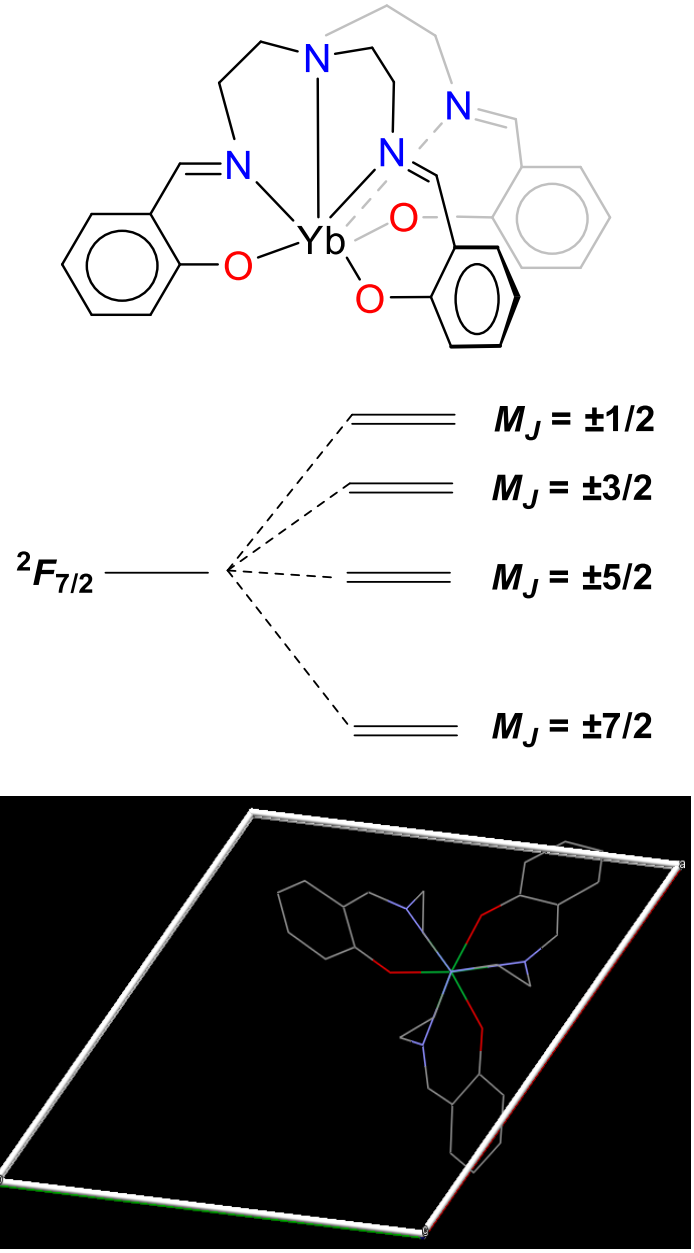

Figure 4.1. (Top) Structure of Yb(trensal) (**4**), (Middle) energy splitting diagram (Bottom) View (looking down the *c* axis) of a molecule of **4** in its crystallographic unit cell; *a* axis: pointing to the top; *b* axis: pointing to the left.

and coworkers reported in 2015 that **4** behaves as a SMM through DC and AC susceptibility measurements.[91] In their studies, **4** was synthesized from the reaction of ytterbium triflate $Yb(OTf)_3$ with salicylaldehyde and tris(2-aminoethyl)amine. The use of lanthanide triflates (rather than lanthanide nitrates as in Ref. 92) was reported earlier by Masatoshi and Toshiro for the preparation of other lanthanide Ln(trensal) complexes.[95]

Crystal structure of **4** at 122(1) K was determined and showed that it is similar to that at 296 K with the trigonal space group *P*-3*c*1 (No. 165).[91, 92] High-resolution absorption and luminescence spectroscopies reveals that the first excited electronic doublet in **4** is nearly 500 cm^{-1} above the ground state.[92] The spin-orbital coupled ground state in an Yb(III) ion is $^2F_{7/2}$. These spectroscopic studies point to the crystal-field splitting in Figure 4.1-Right.

Single-crystal X-band (frequency = 9.62 GHz) EPR spectra of ~5% Yb(III) in Eu(trensal) at 10 K give *g* factors ($g_\parallel$ = 4.29, and $g_\perp$ = 2.90) and hyperfine coupling constants [$A_\parallel^{I=5/2}$ = -0.03123(1) cm^{-1}, $A_\perp^{I=5/2}$ = −0.02244(9) cm^{-1} for ^{173}Yb (I = 5/2, 16% natural abundance); $A_\parallel^{I=1/2}$ = 0.11243(4) cm^{-1}, and $A_\perp^{I=1/2}$ = 0.07407(4) cm^{-1} for ^{171}Yb (I = ½, 14% natural abundance)].

Pedersen and coworkers reported in 2015 that 7% Yb(III) in Lu(trensal) behaves as a chemical qubit.[4] By diluting the complex, the distance between molecules will increase, thereby decreasing intermolecular interactions. When the molecules are far enough apart to minimize the effect of decoherence on the

superposition of states, the compound will exhibit qubit behavior. Otherwise, it exhibits SMM behavior.

4.3. Experimental

4.3.1. Synthesis

Complex **5** was prepared by adding tris(2-aminoethyl)amine to a solution of ytterbium triflate in acetonitrile at 70-80 °C. Salicylaldehyde was added to the solution. The resulting solution was cooled, allowing some of the product to precipitate out. This precipitant was then filtered, washed, and dried. After cooling the filtrate for a few days, microcrystals formed which were ground to make a powder.

Crystals of **4** were prepared by a similar process that involved adding tris(2-aminoethyl)amine to a solution of ytterbium triflate in acetonitrile and refluxing for at least 15 min. The solution was allowed to cool and placed in a 50 mL test tube. Acetonitrile and salicylaldehde were layered on top. After 1 week, single crystals formed. These crystals were collected via filtration, rinsed with acetonitrile, and dried.

4.3.2. FIRMS study

FIRMS studies of **4** were performed in SCM 3 at NHMFL with variable magnetic fields (0-17 T) at 5 K. Transmittance spectra were obtained by barely

covering bottom of the sample well with a powdered sample and then adding eicoseine on top. Instrument parameters were set to default except for the frequency of 7.5 KHz and two 3-min spectra were collected at different magnetic fields in 1 T increments from 0 to 17 T. The crystalline transmittance spectra were collected by covering the sample well with a single layer of small single crystals (Figure 4.2).

4.3.3. Raman magnetospectroscopic study

Raman samples were prepared with unoriented single crystals (Figure 4.2). Data was collected by a backscattering Faraday geometry using a 532 nm laser at SCM 2 (18 T) in the DC Field facility at NHMFL. Crystals of samples were cooled at 4.5 K. Collected scattered light was guided via fiber optics to a spectrometer equipped with a liquid nitrogen-cooled CCD camera.

4.3.4. INS study and computations

VT-INS measurements were taken with a vibrational spectrometer (VISION beamline) in SNS at ORNL. The samples, approximately 0.5 g, were sealed in an aluminum container. The INS spectra of **4** were measured at 5, 25, 50, 75, 100, 125 and 150 K for 1 h at each temperature. The phonon population effect was corrected by normalizing the INS intensity at energy transfer ω with $\coth\left(\frac{\hbar\omega}{2k_BT}\right)$.[56]

Figure 4.2. (Left) Photo of a mosaic of crystals of **4** for far-IR spectroscopy; (Right) Photo of the sample of **4** for Raman magnetospectroscopy.

The crystal-structure information from the CIF file was loaded into VASP and used to generate the input file of phonon frequencies and polarization vectors (also gives irreducible representations). Then, OCLIMAX calculated VISION parameters (generates 0 K spectra). The reported X-ray CIF file of **4** at 100(1) K (CCDC 1044477) was used.[92]

4.4. Results and discussion

4.4.1. FIRMS study

The energy splittings in **4** were studied by the FIRMS technique. This technique employs the Fourier-transform spectrometer to measure the magnetic response from the sample in the frequency domain (down to 20 cm^{-1}) while the magnetic field is fixed. The sample is placed in a cryostat equipped by a vertical bore SCM and coupled to the spectrometer through the evacuated optical beam line. In this manner, the intensity of far-IR radiation transmitted through the sample was recorded with magnetic fields (up to 17 T) and at temperature of 5 K. In all measurements, the magnetic field is applied in Voigt geometry (magnetic field perpendicular to the wave vector of the radiation). All samples were a mixture of the eicosane matrix with microcrystalline powders or a layer of single crystals arranged to cover the sample area held in place by eicosane. The FIRMS spectra and a contour plot of a mosaic of single crystals are shown in Figure 4.3.

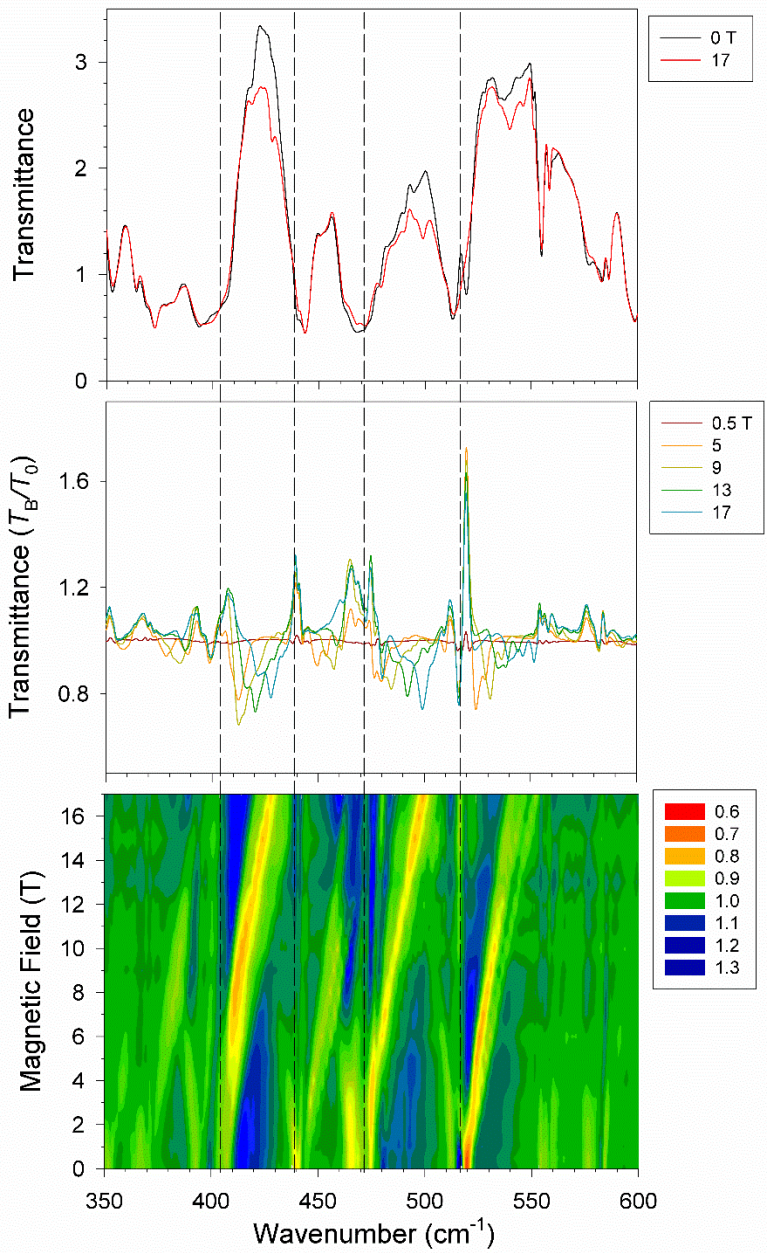

Figure 4.3. (Top) Far-IR spectra of a mosaic of crystals of **4**. (Middle) Transmission normalized to the zero-field spectrum T_B/T_0 at 1-17 T. (Bottom) Contour map of normalized transmission in 0-17 T magnetic fields by the Filled Contour Plot in SigmaPlot 2000. Low-intensity regions indicate the presence of peaks. Each black dotted line indicates the location of a potential phonon.

For the interpretation of far-IR data of **4**, collected data are presented as normalized transmission. The transmission spectrum measured at each magnetic field was normalized to the reference spectrum computed as an averaging of the spectra at all magnetic fields with outlier points removed. Such normalization reveals field-induced features that are otherwise masked in the original (un-normalized) spectra due to the overlaps with phononic or intramolecular vibrational excitations. The quantitative contribution of magnetic excitations to absolute absorption of the sample is determined by the decrease in the normalized transmission. Therefore, this experimentally determined quantity allows direct access to the transition intensity between field-dependent spin energy levels.

For **4**, a magnetic peak at 464 cm^{-1} is expected, corresponding to the splitting between the electronic ground doublet and the first excited crystal field state as determined by luminescence spectroscopy.[91] However, there is no clear indication of this transition in the spectra. Furthermore, the contour plot shows multiple phonon peaks with a repeating pattern, the clearest of which occur at 402.0, 437.0, 470.0, and 515.5 cm^{-1}. This pattern is different from the avoided crossings observed in other SMMs, making it difficult to model.

FIRMS spectra of powders, prepared by grinding crystals of **4**, are shown in Figure 4.4. While the locations of the peaks observed in the normalized transmittance spectra and contour plots in Figures 4.3 and 4.4 are the same, the shifts of the peaks in the contour are different. The far-IR spectra of the powder

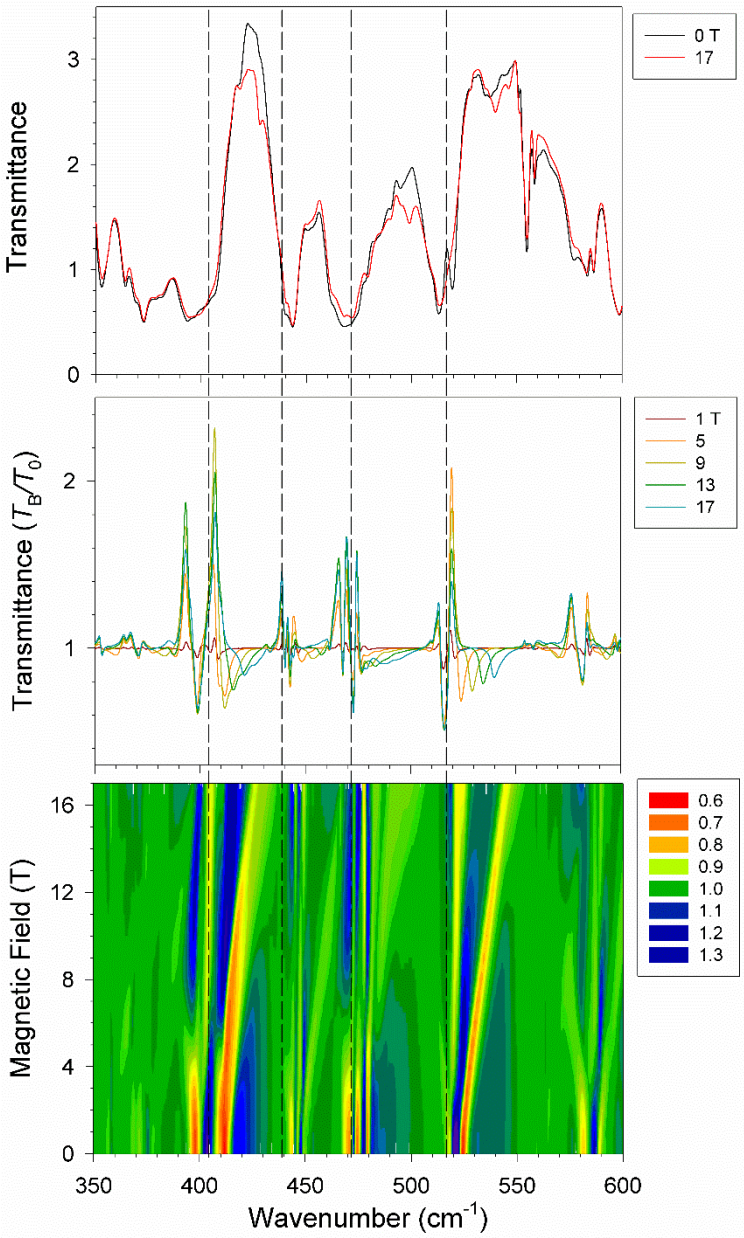

Figure 4.4. (Top) Far-IR spectra of a power sample of **4**. (Middle) Transmission normalized to the zero-field spectrum T_B/T_0 at 1-17 T. (Bottom) Contour map of normalized transmission in 0-17 T magnetic fields by the Filled Contour Plot in SigmaPlot 2000. Low-intensity regions indicate the presence of peaks. Each black dotted line indicates the location of a phonon from Figure 4.3.

and crystal mosaic samples also show several similar features, although there are notable differences between the spectra in Figures 4.3 and 4.4. This is likely due to the difference in orientation between the powder and crystal mosaic samples.

4.4.2. Raman magnetospectroscopic study

Raman spectra for **4** under variable magnetic fields are given in Figure 4.5. No magnetic feature could be identified in the spectra. Even (0, 2, 4….16) fields were collected when increasing the magnetic field during the experiment, and odd fields were collected while decreasing the magnetic field. The difference in spectra is most likely due to magnetic hysteresis (retention of magnetic field) as the field was decreased.

There is a possibility of an interaction with the Raman-active phonon peaks causing the Raman-inactive magnetic peak to show up as a shift in position of the phonon peaks. However, there is no evidence of such a shift despite the presence of multiple phonon peaks in the 350–600 cm^{-1} range.

4.4.3. INS study and phonon computations

INS studies using powder samples of **4** were performed at VISION with variable temperatures. Magnetic transitions, *i.e.*, intramanifold transitions among the crystal-field split KDs within the spin-orbital coupled $^2F_{7/2}$ state are not

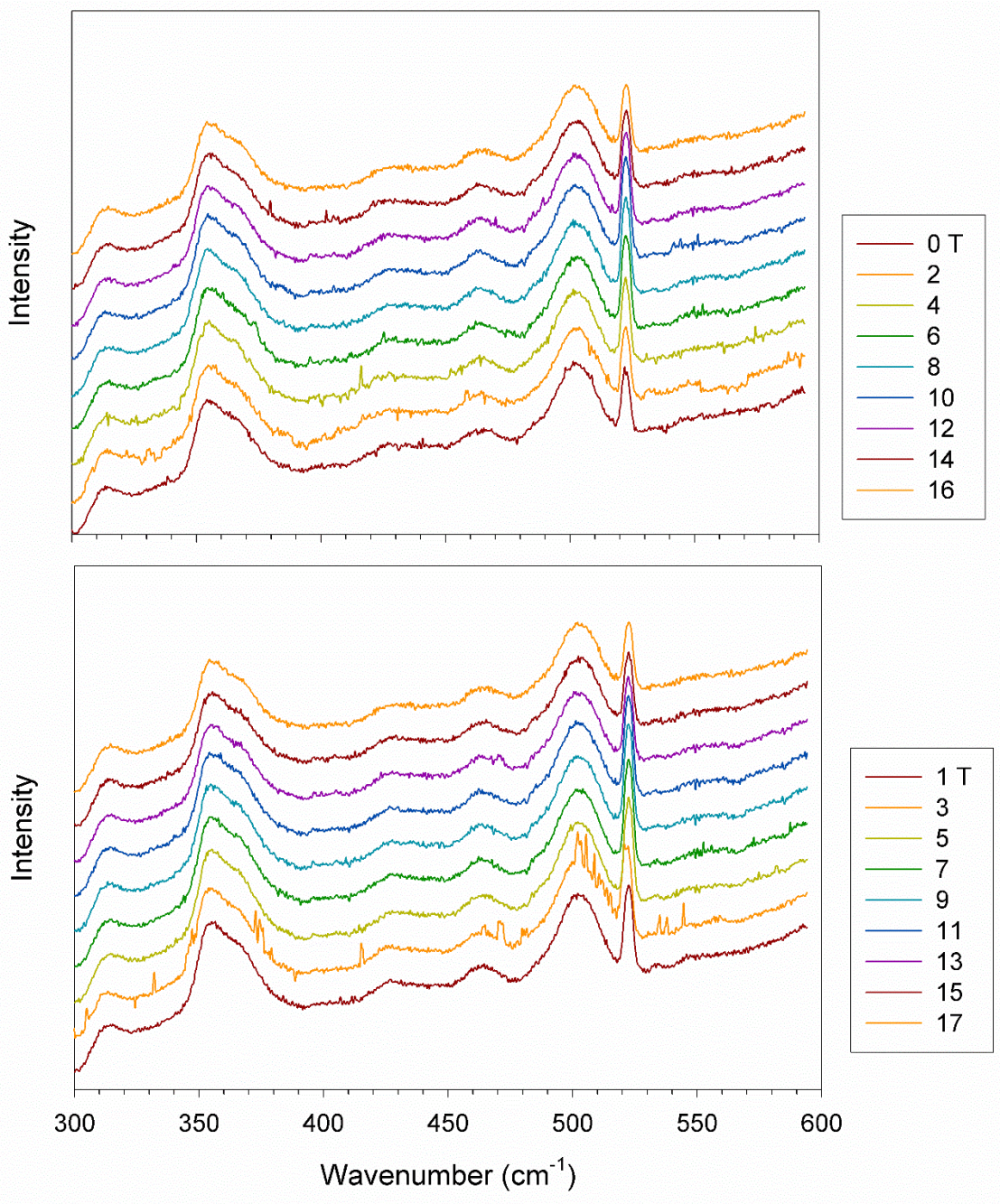

Figure 4.5. Raman spectra of Yb(trensal) (**4**) under external magnetic fields.

obvious from the Bose-corrected forward scattering INS spectra in Figure 4.6.

VASP calculations resulted in a calculated (0 K) spectrum that somewhat matched the experimental (5 K) spectra, albeit with some major discrepancies such as the low frequency region and the double peak near 3,000 cm^{-1}. The symmetry analysis resulted in many phonons being assigned an irreducible representation based upon the C_{2h} symmetry of the crystal. However, most calculated phonons could not be assigned due to the large, complex nature of the system. Based upon the back-scattering intensity of the phonon peaks, we were able to determine the prevalent phonons in the region on interest (350-600 cm^{-1}). These phonons are modeled using Jmol (Animations 9-16).[90] Their intensities and symmetries are given in Table 4.1.

4.5. Conclusions

4 shows a repetitive pattern in FIRMS studies. However, clear differences are shown between powder and crystal samples. Raman spectra do not clearly reveal magnetic features. Furthermore, the intramanifold transitions are not obvious in INS studies. Although the calculated (0 K) spectrum shows very good agreement with the experimental INS data, many of the phonon modes could not be assigned.

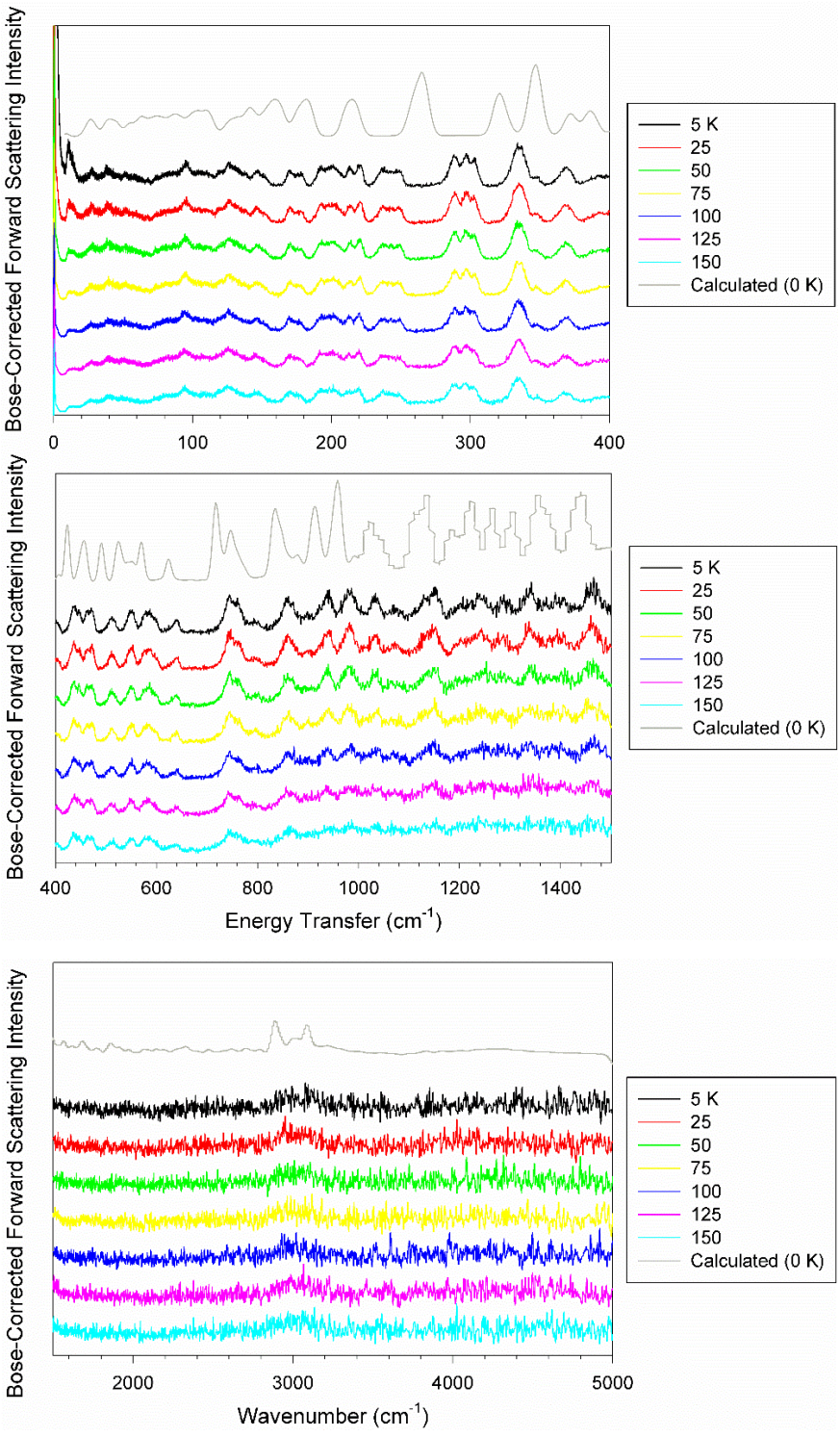

Figure 4.6. INS spectra of **4** at 5, 25, 50, 75, 100, 125 and 150 K on VISION. Calculated 0 K INS spectrum by VASP in grey for comparison**.**

Table 4.1. Animated phonons in Yb(trensal) (**4**) from VASP calculations

Frequency (cm^{-1})	BS Intensity	FS Intensity	Symmetry	Animation File
371.43	0.256(6)	0.177(9)	B_u	9_Complex 4_371.43_Bu.mp4
384.55	0.164(6)	0.113(8)	*N/A*	10_Complex 4_384.53.mp4
407.09	0.101(4)	0.068(0)	A_g	11_Complex 4_407.09_Ag.mp4
423.65	0.348(8)	0.262(9)	*N/A*	12_Complex 4_423.65.mp4
456.15	0.249(4)	0.200(0)	*N/A*	13_Complex 4_456.15.mp4
489.98	0.179(1)	0.141(4)	B_u	14_Complex 4_489.98_Bu.mp4
554.67	0.198(0)	0.166(5)	A_u	15_Complex 4_554.67_Au.mp4
571.57	0.175(7)	0.148(0)	*N/A*	16_Complex 4_571.57.mp4

CHAPTER 5. FUTURE WORK

The research in the current thesis could be expanded upon in several ways.

The first is to perform INS studies and ab-initio computations of phonons in **2**. Temperature-dependent INS studies could provide supporting evidence for the energy of the ZFS transition as well as provide a complete list of phonon energies in the INS spectra. Ab-initio computations of the phonons would confirm these phonon energies as well as give their symmetries.

Secondly, additional FIRMS, Raman, and INS studies of crystal samples of various partially and fully deuterated isotopologues of the dysprosium complex where the acac and/or water ligand is deuterated would complete the studies, providing supporting or contradicting evidence for the theory that deuteration slightly lowers the energy of phonons. FIRMS studies of the partially and fully deuterated isotopologues with a deuterated acac ligand (**3-*d*$_{21}$** and **3-*d*$_{25}$**, respectively) would be performed on crystal samples since the magnetic and phonon peaks as well as their spin-phonon coupling behavior are more clearly visible in spectra of crystal samples than those of powders. Both **3-*d*$_{21}$** and **3-*d*$_{25}$** are more heavily deuterated than the compounds we currently have single-crystal FIRMS studies of (**3** and **3-*d*$_4$**) so any decrease in phonon energy should be more pronounced. Raman magnetospectroscopy studies of dysprosium(III) complexes with either ligand deuterated (**3-*d*$_4$** or **3-*d*$_{21}$**) would provide insight into the magnetic behavior of the Raman-active phonons as well as the effect of deuteration on these peaks. INS studies of the deuterated samples **3-*d*$_4$**, **3-*d*$_{21}$**,

and **3-*d*$_{25}$** may also reveal additional information as the incoherent neutron scattering (and thus background noise in the spectra) is smaller for D atoms than H atoms.

Finally, spectroscopic studies of diluted Yb(III) trensal [7% in Lu(trensal)] could be used to observe how qubit properties differ from the SMM properties of undiluted Yb(trensal). This would require FIRMS, direct optic Raman spectroscopy, VT-INS studies, and VASP computations. Due to the low concentration of this mixture [7% Yb(trensal) in Lu(trensal)], it may be useful to test other dilution levels and see how the magnetic properties change. HF-EPR may also be useful in determining how the energy gaps change with different Yb(III) concentrations in the Yb(III)/Lu(III) mixtures.

REFERENCES

1. Tang, J.; Zhang, P., *Lanthanide Single Molecule Magnets*. Springer, 2015.
2. Frost, J. M.; Harriman, K. L. M.; Murugesu, M., The rise of 3-d single-ion magnets in molecular magnetism: Towards materials from molecules? *Chem. Sci.* **2016,** *7*, 2470-2491.
3. Lapo, B.; Wolfgang, W., Molecular spintronics using single-molecule magnets. *Nat. Mater.* **2008,** *7*, 179.
4. Pedersen, K. S.; Ariciu, A.-M.; McAdams, S.; Weihe, H.; Bendix, J.; Tuna, F.; Piligkos, S., Toward molecular 4f single-ion magnet qubits. *J. Am. Chem. Soc.* **2016,** *138*, 5801.
5. Goswami, S. M., A. K.; Konar, S., Nanoscopic molecular magnets. *Inorg. Chem. Front.* **2015,** *2*, 687-712.
6. Benelli, C.; Gatteschi, D., Single Ion Magnet (SIM). In *Introduction to Molecular Magnetism. From Transition Metals to Lanthanides*, Ch. 13: Wiley-VCH: 2015; pp 217-237.
7. Boča, R., Zero-field splitting in metal complexes. *Coord. Chem. Rev.* **2004,** *248*, 757-815.
8. Craig, G. A.; Murrie, M., 3d single-ion magnets. *Chem. Soc. Rev.* **2015,** *44*, 2135-2147.
9. Demir, S.; Jeon, I.-R.; Long, J. R.; Harris, T. D., Radical ligand-containing single-molecule magnets. *Coord. Chem. Rev.* **2015,** *289*, 149-176.

10. Dey, M.; Gogoi, N., Geometry-mediated enhancement of single-ion anisotropy: A route to single-molecule magnets with a high blocking temperature. *Angew. Chem. Int. Ed.* **2013,** *52*, 12780-12782.

11. Gao, S., Ed., *Molecular Nanomagnets and Related Phenomena*. Springer: 2015.

12. Gatteschi, D.; Sessoli, R., Quantum tunneling of magnetization and related phenomena in molecular materials. *Angew. Chem. Int. Ed.* **2003,** *42*, 268-297.

13. Gatteschi, D.; Sessoli, R.; Villain, J., *Molecular Nanomagnets*. Oxford University Press, 2006.

14. Krzystek, J.; Telser, J., Measuring giant anisotropy in paramagnetic transition metal complexes with relevance to single-ion magnetism. *Dalton Trans.* **2016,** *45*, 16751-16763.

15. Layfield, R. A., Organometallic single-molecule magnets. *Organometallics* **2014,** *33*, 1084-1099.

16. Liu, J.-L.; Chen, Y.-C.; Tong, M.-L., Symmetry strategies for high performance lanthanide-based single-molecule magnets. *Chem. Soc. Rev.* **2018,** *47*, 2431-2453.

17. McInnes, E. J. L.; Winpenny, R. E. P., Molecular Magnets. In *Comprehensive Inorganic Chemistry II*, Poeppelmeier, K., Ed. Elsevier, 2013; pp 371-395.

18. Neese, F.; Pantazis, D. A., What is not required to make a single molecule magnet. *Faraday Discuss.* **2011,** *148*, 229-238.

19. Rinehart, J. D.; Long, J. R., Exploiting single-ion anisotropy in the design of f-element single-molecule magnets. *Chem. Sci.* **2011,** *2*, 2078-2085.

20. Shatruk, M.; Gómez-Coca, S.; Dunbar, K. R., Molecular Magnetism. In *Molecular Magnetic Materials: Concepts and Applications*, Sieklucka, B.; Pinkowicz, D., Eds. Wiley-VCH, 2017; pp 29-77.

21. Stavretis, S. E.; Mamontov, E.; Moseley, D. H.; Cheng, Y.; Daemen, L. L.; Ramirez-Cuesta, A. J.; Xue, Z.-L., Effect of magnetic fields on the methyl rotation in a paramagnetic cobalt(II) complex. Quasielastic neutron scattering studies. *Phys. Chem. Chem. Phys.* **2018,** *20*, 21119-21126.

22. Yamashita, M.; Katoh, K., Single Molecule Magnets. In *Molecular Magnetic Materials: Concepts and Applications*, Sieklucka, B.; Pinkowicz, D., Eds. Wiley-VCH, 2017; pp 79-101.

23. Zhang, P.; Zhang, L.; Tang, J., Lanthanide single molecule magnets: Progress and perspective. *Dalton Trans.* **2015,** *44*, 3923-3929.

24. Gómez-Coca, S.; Urtizberea, A.; Cremades, E.; Alonso, P. J.; Camón, A.; Ruiz, E.; Luis, F., Origin of slow magnetic relaxation in Kramers ions with non-uniaxial anisotropy. *Nat. Commun.* **2014,** *5*, 4300.

25. Chen, L.; Wang, J.; Wei, J.-M.; Wernsdorfer, W.; Chen, X.-T.; Zhang, Y.-Q.; Song, Y.; Xue, Z.-L., Slow magnetic relaxation in a mononuclear eight-coordinate cobalt(II) complex. *J. Am. Chem. Soc.* **2014,** *136*, 12213-12216.

26. Stavretis, S. E. A., M.; Podlesnyak, A. A.; Hunter, S. C.; Neese, F.; Xue, Z.-L., Magnetic transitions in iron porphyrin halides by inelastic neutron scattering and ab initio studies of zero-field splittings. *Inorg. Chem.* **2015,** *54*.

27. Markus P. Hehlen, M. G. B., Karl W. Gramer, 50th anniversary of the Judd-Ofelt theory: An experimentalist's view of the formalism and its application. *J. Lumin.* **2013,** *136*, 221-239.

28. Peijzel, P. S.; Meijerink, A.; Wegh, R. T.; Reid, M. F.; Burdick, G. W., A complete $4f^n$ energy level diagram for all trivalent lanthanide ions. *J. Solid State Chem.* **2005,** *178*, 448-453.

29. Dieke, G. H.; Crosswhite, H. M., The spectra of the doubly and triply ionized rare earths. *Appl. Op.* **1963,** *2*, 675-686.

30. de Bettencourt-Dias, A., The Electronic Structure of the Lanthanides. In *Encyclopedia of Inorganic and Bioinorganci Chemistry*, Wiley, 2012; pp 1-8.

31. Day, B. M.; Guo, F.-S.; Layfield, R. A., Cyclopentadienyl ligands in lanthanide single-molecule magnets: One ring to rule them all? *Acc. Chem. Res.* **2018,** *51*, 1880-1889.

32. Liddle, S. T.; Van Slageren, J., Improving f-element single molecule magnets. *Chem. Soc. Rev.*, **2015**, *44*, 6655-6669.

33. McAdams, S. G.; Ariciu, A.-M.; Kostopoulos, A. K.; Walsh, J. P. S.; Tuna, F., Molecular single-ion magnets based on lanthanides and actinides: Design considerations and new advances in the context of quantum technologies. *Coord. Chem. Rev.* **2017,** *346*, 216-239.

34. Marx, R.; Moro, F.; Drfel, M.; Ungur, L.; Waters, M.; Jiang, S. D.; Orlita, M.; Taylor, J.; Frey, W.; Chibotaru, L. F.; Van Slageren, J., Spectroscopic determination of crystal field splittings in lanthanide double deckers. *Chem. Sci.* **2014,** *5*, 3287-3293.

35. Liu, J.; Meng, Y.; Hlavicka, I.; Orlita, M.;Jiang, S. D.; Wang, B.; Gao, S., Determination of zero-field splitting in Co^{2+} halide complexes with magnetic and far-IR measurements. *Dalton Trans.* **2017,** *46*, 7408-7411.

36. Byrnes, J., Unexploded ordnance detection and mitigation. Springer, 2009; pp. 21-22.

37. Rechkemmer, Y.; Breitgoff, F. D.; van der Meer, M.; Atanasov, M.; Hakl, M.; Orlita, M.; Neugebauer, P.; Neese, F.; Sarkar, B.; van Slageren, J., A four-coordinate cobalt(II) single-ion magnet with coercivity and a very high energy barrier. *Nat. Commun.* **2016,** *7*, 10467.

38. Moseley, D. H.; Stavretis, S. E.; Thirunavukkuarasu, K.; Ozerov, M.; Cheng, Y.; Daemen, L. L.; Ludwig, J.; Lu, Z.; Smirnov, D.; Brown, C. M.; Pandey, A.; Ramirez-Cuesta, A. J.; Lamb, A. C.; Atanasov, M.; Bill, E.; Neese, F.; Xue, Z.-L., Spin–phonon couplings in transition metal complexes with slow magnetic relaxation. *Nat. Commun.* **2018,** *9*, 2572.

39. Stavretis, S. E.; Moseley, D. H.; Fei, F.; Cui, H.-H.; Cheng, Y.; Podlesnyak, A. A.; Wang, X.; Daemen, L. L.; Hoffmann, C. M.; Ozerov, M.; Lu, Z.; Thirunavukkuarasu, K.; Smirnov, D.; Chang, T.; Chen, Y.-S.; Ramirez-Cuesta, A. J.; Chen, X.-T.; Xue, Z.-L., Spectroscopic studies of the magnetic excitation and spin-phonon couplings in a single-molecule magnet. *Chem. Eur. J.* **2019,** *25*, 15846-15857.

40. Ray, K.; Begum, A.; Weyhermüller, T.; Piligkos, S.; van Slageren, J.; Neese, F.; Wieghardt, K., The electronic structure of the isoelectronic, square-planar complexes $[Fe^{II}(L)_2]^{2-}$ and $[Co^{III}(LBu)_2]^{-}$ (L^{2-} and $(LBu)^{2-}$ = benzene-1,2-dithiolates): An experimental and density functional theoretical study. *J. Am. Chem. Soc.* **2005,** *127*, 4403-4415.

41. Rechkemmer, Y.; Fischer, J. E.; Marx, R.; Dörfel, M.; Neugebauer, P.; Horvath, S.; Gysler, M.; Brock-Nannestad, T.; Frey, W.; Reid, M. F.; van Slageren, J., Comprehensive spectroscopic determination of the crystal field splitting in an erbium single-ion magnet. *J. Am. Chem. Soc.* **2015,** *137*, 13114-13120.

42. Bunting, P. C.; Atanasov, M.; Damgaard-Møller, E.; Perfetti, M.; Crassee, I.; Orlita, M.; Overgaard, J.; van Slageren, J.; Neese, F.; Long, J. R., A linear cobalt(II) complex with maximal orbital angular momentum from a non-Aufbau ground state. *Science* **2018,** *362*, eaat7319.

43. Jiang, S.-D.; Maganas, D.; Levesanos, N.; Ferentinos, E.; Haas, S.; Thirunavukkuarasu, K.; Krzystek, J.; Dressel, M.; Bogani, L.; Neese, F.; Kyritsis, P., Direct observation of very large zero-field splitting in a tetrahedral $Ni^{II}Se_4$ coordination complex. *J. Am. Chem. Soc.* **2015,** *137*, 12923-12928.

44. Świtlicka, A.; Machura, B.; Penkala, M.; Bieńko, A.; Bieńko, D. C.; Titiš, J.; Rajnák, C.; Boča, R.; Ozarowski, A.; Ozerov, M., Slow magnetic relaxation in cobalt(II) field-induced single-ion magnets with positive large anisotropy. *Inorg. Chem.* **2018,** *57*, 12740-12755.

45. Hay, M. A.; Sarkar, A.; Craig, G. A.; Bhaskaran, L.; Nehrkorn, J.; Ozerov, M.; Marriott, K. E. R.; Wilson, C.; Rajaraman, G.; Hill, S.; Murrie, M., In-depth investigation of large axial magnetic anisotropy in monometallic 3d complexes using frequency domain magnetic resonance and ab initio methods: A study of trigonal bipyramidal Co(II). *Chem. Sci.* **2019,** *10*, 6354-6361.

46. Haas, S., Far-infrared spectroscopy of lanthanide-based molecular magnetic materials, Ph.D. dissertation. University of Stuttgart, 2015.

47. Brackett, G., Far-infrared magnetic resonance in Fe(III) and Mn(III) porphyrins, myoglobin, hemoglobin, ferrichrome A, and Fe(III) dithiocarbamates. Ph.D. dissertation. University of California at Berkeley, 1970.

48. Brackett, G. C.; Richards, P. L.; Caughey, W. S., Far-infrared magnetic resonance in Fe(III) and Mn(III) porphyrins, myoglobin, hemoglobin, ferrichrome A, and Fe(III) dithioncarbamates. *J. Chem. Phys.* **1971,** *54*, 4383-4401.

49. Luo, W., Campbell, P. G.; Zakharov, L.N.; Liu, S.-Y., A single-component liquid-phase hydrogen storagematerial. *J. Am. Chem. Soc.* **2011,** *133*, 19326-19329.

50. North, J. M.; Dalal, N. S., Raman and infrared modes of the single molecule magnet Fe_8Br_8 and analogs. *J. Appl. Phys.* **2003,** *93*, 7092-7094.

51. Clark, R.; Dines, T., Electronic Raman Spectroscopy. In *Advances in Infrared and Raman Spectroscopy*, Clark, R.; Hester, R., Eds. Heyden, 1982; Vol. 9, pp 282-360.

52. Gorller-Walrand, C.; Binnemans, K., Spectral Intensities of f-f Transitions. In *Handbook on the Physics and Chemistry of Rare Earths*, K. Gschneidner, J.; Eyring, L., Eds. Elsevier, 1998; Vol. 25.

53. Dunstan, M. A.; Mole, R. A.; Boskovic, C., Inelastic neutron scattering of lanthanoid complexes and single-molecule magnets. *Eur. J. Inorg. Chem.* **2019**, 1050-1105.

54. Basler, R.; Boskovic, C.; Chaboussant, G.; Güdel, H. U.; Murrie, M.; Ochsenbein, S. T.; Sieber, A., Molecular spin clusters: New synthetic approaches and neutron scattering studies. **2003,** *4*, 910-926.

55. Furrer, A. M., J.; Strässle, T., Neutron Scattering in Condensed Matter Physics. *World Scientific Publishing Company* **2008**.

56. Mitchell, P. C. H.; Parker, S. F.; Ramirez-Cuesta, A. J.; Tomkinson, J., *Vibrational Spectroscopy with Neutrons. With Applications in Chemistry, Biology, Materials Science and Catalysis*. World Scientific Publishing Company: 2005.

57. Dove, M. T., *Introduction to Lattice Dynamics*. Cambridge University Press: 1993.

58. Schwoerer; M.; Wolf, H. C., Organic Molecular Solid. Wiley-VCH: 2007; pp 89-124.

59. Giansiracusa, M. J.; Vonci, M.; Van Den Heuvel, W.; Gable, R. W.; Moubaraki, B.; Murray, K. S.; Yu, D.; Mole, R. A.; Soncini, A.; Boskovic, C., Carbonate-bridged lanthanoid triangles: Single-molecule magnet behavior, ielastic neutron scattering, and ab initio studies. *Inorg. Chem.* **2016,** *55*, 5201.

60. Vonci, M.; Giansiracusa, M. J.; Gable, R. W.; Van Den Heuvel, W.; Latham, K.; Moubaraki, B.; Murray, K. S.; Yu, D.; Mole, R. A.; Soncini, A.; Boskovic, C., Ab initio calculations as a quantitative tool in the inelastic neutron scattering study of a single-molecule magnet analogue. *Chem. Comm.* **2016,** *52*, 2091-2094.

61. The Vienna Ab-initio Simulation Package: Atomic scale materials modelling from first principles. https://www.vasp.at.

62. McKinnon, J. J.; Jayatilaka, D.; Spackman, M. A., Towards quantitative analysis of intermolecular interactions with Hirshfeld surfaces. *Chem. Commun.* **2007**, 3814-3816.

63. Spackman, M. A.; Jayatilaka, D., Hirshfeld surface analysis. *Cryst. Eng. Comm.* **2009,** *11*, 19-32.

64. Spackman, M. A.; McKinnon, J. J., Fingerprinting intermolecular interactions in molecular crystals. *Cryst. Eng. Comm.* **2002,** *4*, 378-392.

65. McKinnon, J. J.; Spackman, M. A.; Mitchell, A. S., Novel tools for visualizing and exploring intermolecular interactions in molecular crystals. *Acta Cryst. B* **2004,** *60*, 627-668.

66. Turner, M. J.; McKinnon, J. J.; Jayatilaka, D.; Spackman, M. A., Visualisation and characterisation of voids in crystalline materials. *Cryst. Eng. Comm.* **2011,** *13*, 1804-1813.

67. Hunter, S. C.; Smith, B. A.; Hoffmann, C. M.; Wang, X.; Chen, Y.-S.; McIntyre, G. J.; Xue, Z.-L., Intermolecular interactions in solid-state metalloporphyrins and their impacts on crystal and molecular structures. *Inorg. Chem.* **2014,** *53*, 11552-11562.

68. Bone, A. N.; Stavretis, S. E.; Krzystek, J.; Liu, Z.; Chen, Q.; Gai, Z.; Wang, X.; Steren, C. A.; Powers, X. B.; Podlesnyak, A. A.; Chen, X.-T.; Telser, J.; Zhou, H.; Xue, Z.-L., Manganese tetraphenylporphyrin bromide and iodide. Studies of structures and magnetic properties, *Polyhedron* **2020**, *184*, 114488.

69. Ruamps, R.; Maurice, R.; Batchelor, L.; Boggio-Pasqua, M.; Guillot, R.; Barra, A. L.; Liu, J.; Bendeif, E.-E.; Pillet, S.; Hill, S.; Mallah, T.; Guihéry, N., Giant ising-type magnetic anisotropy in trigonal bipyramidal Ni(II) complexes: Experiment and theory. *J. Am. Chem. Soc.* **2013,** *135*, 3017.

70. Feng, M.; Tong, M.-L., Single ion magnets from 3d to 5f: Developments and strategies. *Chem. Eur. J.* **2018**, *24*, 7574-7594.

71. Rinehart, J. D.; Long, J. R., Exploiting single-ion anisotropy in the design of *f*-element single-molecule magnets. *Chem. Sci.* **2011,** *2*, 2078-2085.

72. Marriott, K. E. R.; Bhaskaran, L.; Wilson, C.; Medarde, M.; Ochsenbein, S. T.; Hill, S.; Murrie, M., Pushing the limits of magnetic anisotropy in trigonal bipyramidal Ni(II). *Chem. Sci.* **2015,** *6*, 6823-6828.

73. Miklovič, J.; Valigura, D.; Boča, R.; Titiš, J., A mononuclear Ni(II) complex: A field induced single-molecule magnet showing two slow relaxation processes. *Dalton Trans.* **2015,** *44*, 12484-12487.

74. Lomjanský, D.; Moncol, J.; Rajnák, C.; Titiš, J.; Boča, R., Field effects to slow magnetic relaxation in a mononuclear Ni(II) complex. *Chem. Commun.* **2017,** *53*, 6930-6932.

75. Craig, G. A.; Sarkar, A.; Woodall, C. H.; Hay, M. A.; Marriott, K. E. R.; Kamenev, K. V.; Moggach, S. A.; Brechin, E. K.; Parsons, S.; Rajaraman, G.; Murrie, M., Probing the origin of the giant magnetic anisotropy in trigonal bipyramidal Ni(II) under high pressure. *Chem. Sci.* **2018,** *9*, 1551-1559.

76. Titiš, J.; Rajnák, C.; Valigura, D.; Boča, R., Field influence on the slow magnetic relaxation of nickel-based single ion magnets. *Dalton Trans.* **2018,** *47*, 7879-7882.

77. Titiš, J.; Chrenková, V.; Rajnák, C.; Moncol, J.; Valigura, D.; Boča, R., Exceptionally slow magnetic relaxation in a mononuclear hexacoordinate Ni(II) complex. *Dalton Trans.* **2019,** *48*, 11647-11650.

78. Rudowicz, C.; Açıkgöz, M.; Gnutek, P., Superposition model analysis of nickel(II) ions in trigonal bipyramidal complexes exhibiting huge zero field splitting (aka ‘giant magnetic anisotropy’). *J. Magn. Magn. Mater.* **2017,** *434*, 56-61.

79. Turner, M. J.; McKinnon, J. J.; Wolff, S. K.; Grimwood, D. J.; Spackman, P. R.; Jayatilaka, D.; Spackman, M. A. CrystalExplorer17. https://crystalexplorer.scb.uwa.edu.au/

80. Stoll, S.; Schweiger, A., EasySpin, a comprehensive software package for spectral simulation and analysis in EPR. *J. Magn. Reson.* **2006,** *178*, 42-55.

81. Fingerprint plots; Website: http://crystalexplorer.scb.uwa.edu.au/wiki/index.php/Fingerprint_Plots.

82. Colacio, E.; Ruiz, J.; Ruiz, E.; Cremades, E.; Krzystek, J.; Carretta, S.; Cano, J.; Guidi, T.; Wernsdorfer, W.; Brechin, E. K., Slow magnetic relaxation in a Co^{II}–Y^{III} single-ion magnet with positive axial zero-field splitting. *Angew. Chem. Int. Ed.* **2013,** *52*, 9130.

83. Hirshfeld surface properties; Web site: http://crystalexplorer.scb.uwa.edu.au/wiki/index.php/Surface_Properties.

84. Kamiguchi, S.; Takahashi, I.; Kondo, K.; Nagashima, S.; Kurokawa, H.; Miura, H.; Chihara, T., Catalytic hydration of alkynes over Brønsted acid sites developed on halide clusters. *J. Clust. Sci.* **2007,** *18*, 845-853.

85. Marchetti, F.; Pampaloni, G.; Zacchini, S., Reactivity of niobium and tantalum pentahalides with cyclic ethers and the isolation and characterization of intermediates in the polymerization of tetrahydrofuran. *Inorg. Chem.* **2008,** *47*, 365-372.

86. Jiang, S.-D.; Wang, B.-W.; Su, G.; Wang, Z.-M.; Gao, S., A mononuclear dysprosium complex featuring single-molecule-magnet behavior. *Angew. Chem.* **2010,** *122*, 7610-7613.

87. Jiang, S.-D.; Wang, B.-W.; Su, G.; Wang, Z.-M.; Gao, S., A mononuclear dysprosium complex featuring single-molecule magnet behavior. *Angew. Chem. Int. Ed.* **2010,** *49*, 7448–7451.

88. Liu, J.; Chen, Y.-C.; Liu, J.-L.; Vieru, V.; Ungur, L.; Jia, J.-H.; Chibotaru, L. F.; Lan, Y.; Wernsdorfer, W.; Gao, S.; Chen, X.-M.; Tong, M.-L., A stable pentagonal bipyramidal Dy(III) single-ion magnet with a record magnetization reversal barrier over 1000 K. *J. Am. Chem. Soc.* **2016,** *138*, 5441-5450.

89. Frediani, P. R., D.; Muniz-Miranda, M.; Salvini, A.; Caporali, M., An easy way to perdeuterated pyrazoles by catalytic exchange reactions. *Catal. Commun.* **2001,** *2*, 125-128.

90. Jmol: An opensource Java viewer for chemical structures in 3D. http://www.jmol.org/.

91. Pedersen, K. S.; Dreiser, J.; Weihe, H.; Sibille, R.; Johannesen, H. V.; Sørensen, M. A.; Nielsen, B. E.; Sigrist, M.; Mutka, H.; Rols, S.; Bendix, J.; Piligkos, S., Design of single-molecule magnets: Insufficiency of the anisotropy barrier as the sole criterion. *Inorg. Chem.* **2015,** *54*, 7600-7606.

92. Bernhardt, P. V.; Flanagan, B. M.; Riley, M. J., Completion of the isomorphous Ln(trensal) series. *Aust. J. Chem.* **2001,** *54*, 229-232.

93. Costes, J.-P.; Dupuis, A.; Commenges, G.; Lagrave, S.; Laurent, J.-P., Mononuclear lanthanide complexes of tripodal ligands: Synthesis and spectroscopic studies. *Inorg. Chim. Acta* **1999,** *285*, 49-54.

94. Bernhardt, P. V.; Flanagan, B. M.; Riley, M. J.; Wood, B. J., An XPS study of an isomorphous trivalent lanthanoid series. *J. Electron. Spectros. Relat. Phenomena* **2002,** *124*, 73-77.

95. Masatoshi, K.; Toshiro, Y., Synthesis and structural characterization of Ln(III) complexes (Ln = Eu, Gd, Tb, Er, Tm, Lu) of tripodal tris[2(salicylideneamino)ethyl]amine. *Chem. Lett.* **1999,** *28*, 137-138.

APPENDIX

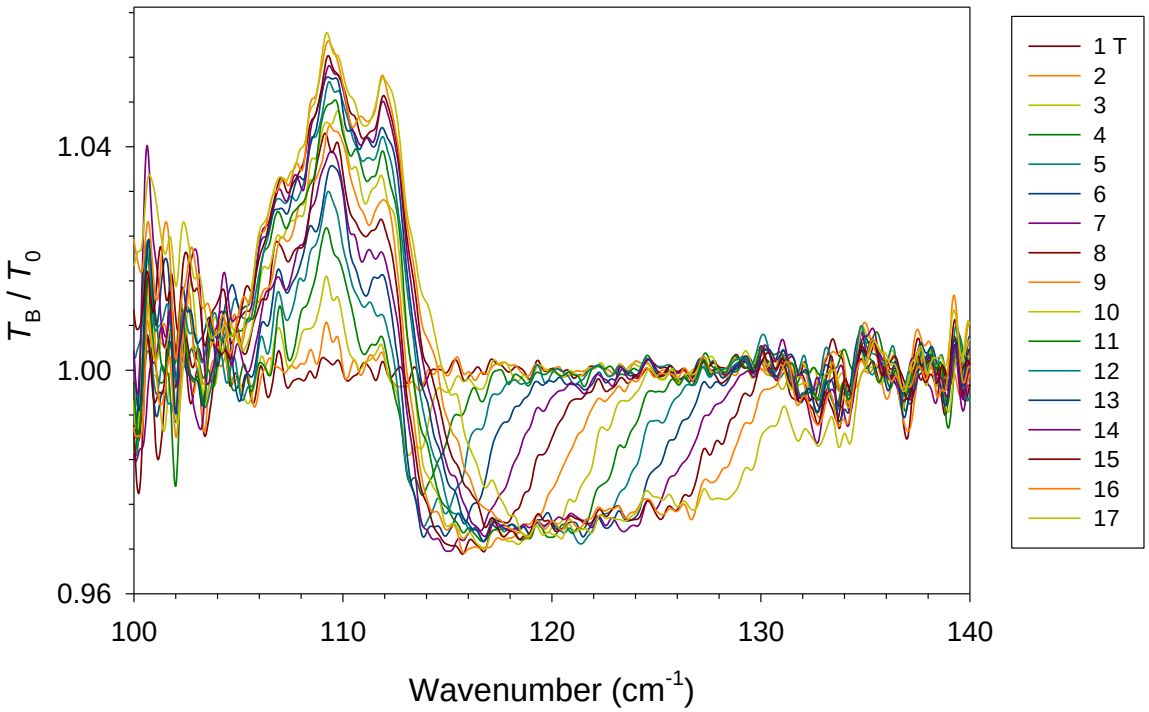

Figure A1. Transmission FIRMS of **2** normalized to the zero-field spectrum T_B/T_0 at 1-17 T.

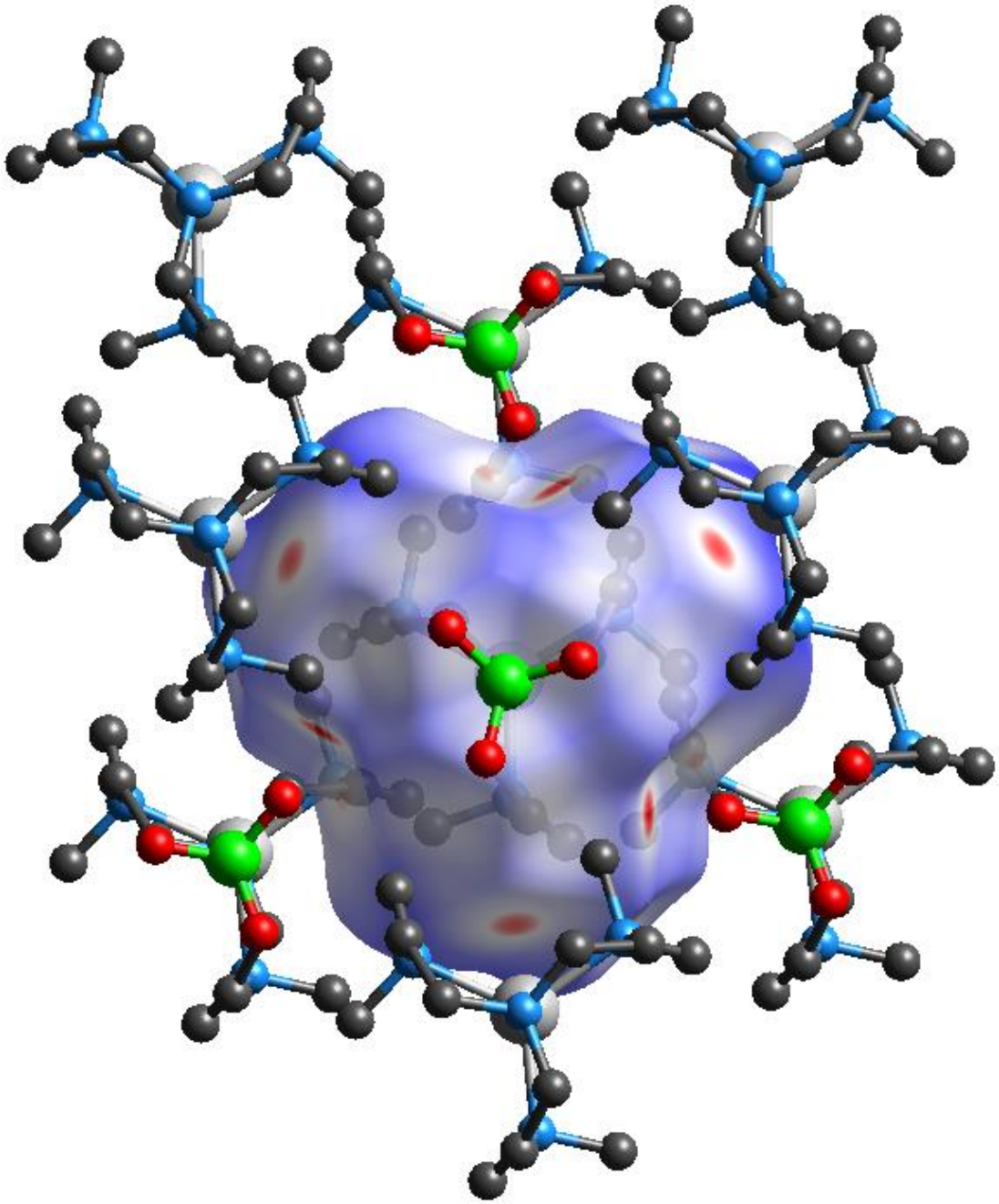

Figure A2. Additional top view of the Hirshfeld surface of **2** showing the packing diagram.

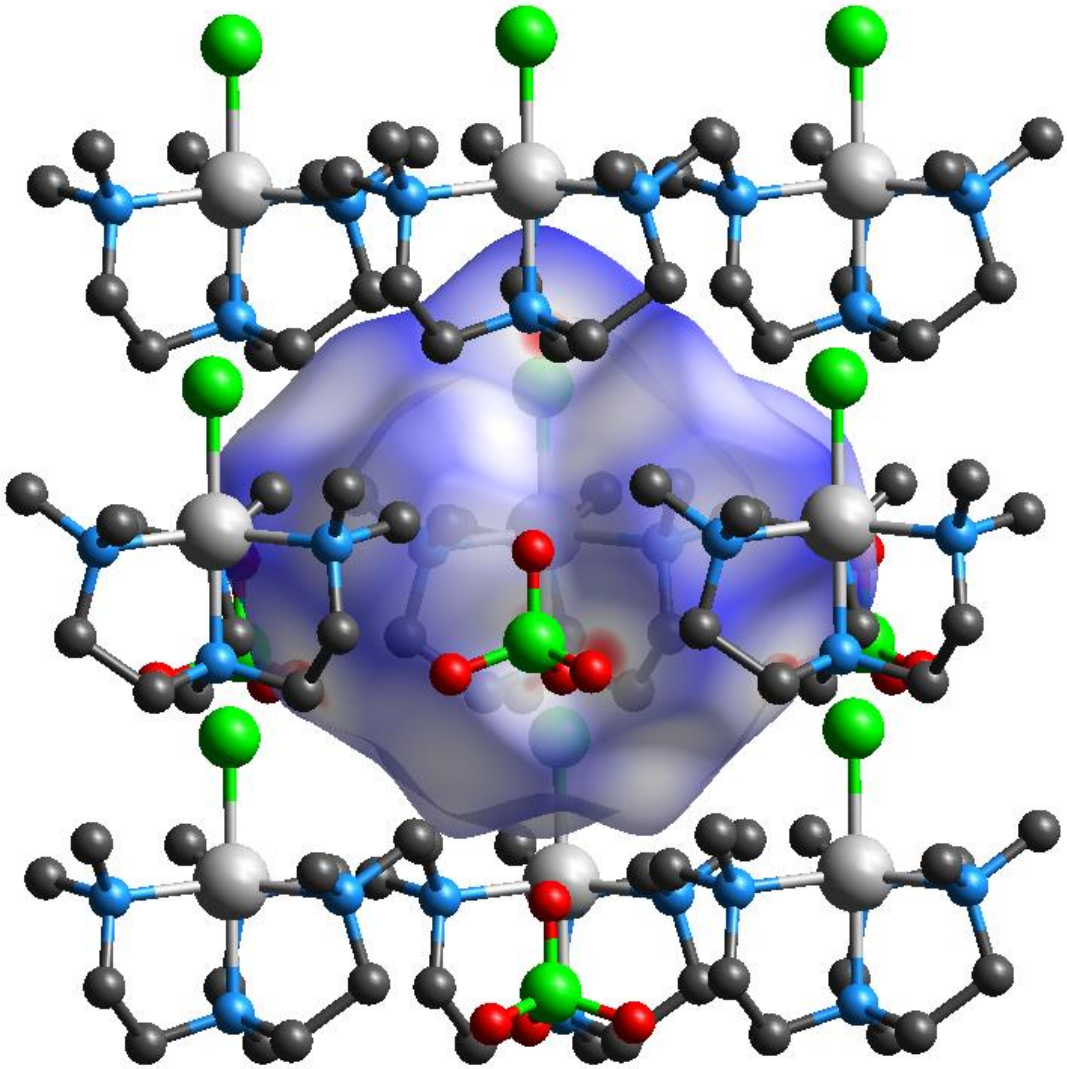

Figure A3. Additional side view of the Hirshfeld surface of **2** showing the packing diagram.

VITA

Chelsea N. Widener was born in Savannah, GA. She enrolled in Wesleyan College (Macon, GA) in 2011. Chelsea conducted undergraduate research on heavy metals in natural water sources at Wesleyan, multi-graft block copolymer heterogeneity in the Center for Nanophase Materials Science at Oak Ridge National Laboratory, effects of carbon sequestration on minerals in the soil at Pacific Northwest National Laboratory, and the statistical fairness of online gambling at Wesleyan College. Chelsea graduated in 2015 with a double major in chemistry and applied mathematical science. She completed one semester of graduate mathematics courses at Auburn University (Auburn, AL). Chelsea then taught high school chemistry and mathematics in Macon, GA. She began her graduate studies in inorganic chemistry at the University of Tennessee-Knoxville in August 2017.